Data-driven Methods in Mechanical Model Calibration and Prediction for Mesostructured Materials

Jee Yun Kim

Thesis submitted to the faculty of the Virginia Polytechnic Institute and State University in partial fulfillment of the requirements for the degree of

Master of Science

In

Materials Science and Engineering

Hang Yu, Chair

David Higdon

Zhenyu Kong

8/29/2018

Blacksburg, Virginia

Keywords: Materials Design; Model Prediction; Uncertainty Quantification; Data-Driven Approaches; Mechanics

Data-driven Methods in Mechanical Model Calibration and Prediction for Mesostructured Materials

Jee Yun Kim

ABSTRACT

Mesoscale design involving control of material distribution pattern can create a statistically heterogeneous material system, which has shown increased adaptability to complex mechanical environments involving highly non-uniform stress fields. Advances in multi-material additive manufacturing can aid in this mesoscale design, providing voxel level control of material property. This vast freedom in design space also unlocks possibilities within optimization of the material distribution pattern. The optimization problem can be divided into a forward problem focusing on accurate predication and an inverse problem focusing on efficient search of the optimal design. In the forward problem, the physical behavior of the material can be modeled based on fundamental mechanics laws and simulated through finite element analysis (FEA). A major limitation in modeling is the unknown parameters in constitutive equations that describe the constituent materials; determining these parameters via conventional single material testing has been proven to be insufficient, which necessitates novel and effective approaches of calibration.

A calibration framework based in Bayesian inference, which integrates data from simulations and physical experiments, has been applied to a study involving a mesostructured material fabricated by fused deposition modeling. Calibration results provide insights on what values these parameters converge to as well as which material parameters the model output has the largest dependence on while accounting for sources of uncertainty introduced during the modeling process. Additionally, this statistical formulation is able to provide quick predictions of the physical system by implementing a surrogate and discrepancy model. The surrogate model is meant to be a statistical representation of the simulation results, circumventing issues arising from computational load, while the discrepancy is aimed to account for the difference between the simulation output and physical experiments. In this thesis, this Bayesian calibration framework is applied to a material bending problem, where in-situ mechanical characterization data and FEA simulations based on constitutive modeling are combined to produce updated values of the unknown material parameters with uncertainty.

Data-driven Methods in Mechanical Model Calibration and Prediction for Mesostructured Materials

Jee Yun Kim

GENERAL AUDIENCE ABSTRACT

A material system obtained by applying a pattern of multiple materials has proven its adaptability to complex practical conditions. The layer by layer manufacturing process of additive manufacturing can allow for this type of design because of its control over where material can be deposited. This possibility then raises the question of how a multi-material system can be optimized in its design for a given application. In this research, we focus mainly on the problem of accurately predicting the response of the material when subjected to stimuli. Conventionally, simulations aided by finite element analysis (FEA) were relied upon for prediction, however it also presents many issues such as long run times and uncertainty in context-specific inputs of the simulation. We instead have adopted a framework using advanced statistical methodology able to combine both experimental and simulation data to significantly reduce run times as well as quantify the various uncertainties associated with running simulations.

ACKNOWLEDGEMENTS

I would first like to thank my advisor, Dr. Hang Yu, for all of his guidance which made this research possible. I would like to thank Dr. David Higdon for his patience and help with my understanding of the research. I would like to thank Dr. Zhenyu Kong for this input and support. I would also like to thank Mr. David Garcia, for the help that he has given throughout my research with data collection. I would like to thank my colleagues in my research group for their continued support. Finally, I would like to thank the Materials Science and Engineering department for their administrative support.

ATTRIBUTION

A colleague aided in the data collection and research for one of the chapters within this thesis. Their contribution is briefly described here.

Chapter 2: Physical Experiments & Model Development and Simulations.

David Garcia is currently a Ph.D. candidate under Dr. Hang Yu. David helped with the characterization of the mesostructure and development of the finite element model.

Table of Contents

Table of Contents vi

List of Figures viii

List of Tables x

Chapter 1: Introduction 1

Chapter 2: Literature Review 3

2.1 Mesoscale Heterogeneous Material Systems 3
2.2 Multi-Material Additive Manufacturing 4
2.3 Constitutive Modeling and Simulations 5
2.4 Computer Model Uncertainty and Model Calibration 7
2.5 Local Deformation Characterization via Digital Image Correlation 8
2.6 Overview of Bayesian Inference 9
2.7 Overview of Gaussian Process 10
2.8 Gaussian Process Surrogate Model 12
2.9 Singular Value Decomposition 15
2.10 Basis Representation 16
2.11 Markov Chain Monte Carlo Methods 16
2.12 Univariate Model Formulation 19

Chapter 3: Experimental 23

3.1 Calibration Framework Overview 23
3.2 Physical Experiments 24
3.3 Model Development and Simulations 27
3.3.1 Constitutive Modeling 27
3.3.2 Finite Element Analysis Simulations 29
3.4 Bayesian Calibration 34
3.4.1 Surrogate Model Formulation 34
3.4.2 Discrepancy Model Formulation 36
3.4.3 Complete Model Formulation 38
3.4.1 Predictions 40

Chapter 4: Results & Discussion 42
4.1 Training Plan 1 42
4.2 Training Plan 2 53
Chapter 5: Conclusions 62
Resources 63

List of Figures

Figure 1. Forward and inverse problems of multi-material mechanical design. The highlighted portion is the focus of this thesis..... 2
Figure 2. Bayesian calibration framework..... 24
Figure 3. Five material distributions samples were fabricated at for mechanical testing..... 25
Figure 4. Experimental results of the maximum displacements for each mesostructured sample 26
Figure 5. Maximum tangential strain distribution obtained by DIC of full TPU beam (left) and mesostructured 46% nylon beam (right) at the same time step 27
Figure 6. Stress-strain curve for nylon material (a) and stress-strain curve for TPU (b) obtained from uniaxial tension testing..... 28
Figure 7. Representative simulation results of a 27% nylon design 30
Figure 8. Scatter plot matrix of o_1=176 LH design for validation set (a) and o_2=200 Latin Hypercube design for training set (b) 32
Figure 9. Simulation output of $m = 131$ runs..... 33
Figure 10. Scatter plot matrix of designs removed from training set 34
Figure 11. $p\eta = 2$ principal components used for formulating surrogate model..... 35
Figure 12. Boxplots of posterior realizations of ρwik parameter for each principal component 42
Figure 13. Surrogate model hold-out residuals..... 44
Figure 14. Sensitivity analysis of variable and calibration inputs 44
Figure 15. Posterior mean surface of basis weight $w_1(x, \boldsymbol{t})$ with varied θ_1 and θ_3 values (left) and varied θ_1 and θ_4 (right) 45
Figure 16. Posterior MCMC realizations of calibration inputs..... 47
Figure 17. Comparison of surrogate model mean response (blue) and simulation output (green)48
Figure 18. Posterior hold-out predictions at each experimental input. First column: 5th and 95th percentile bounds of surrogate model response (green) and experimental data (blue). Second column: 5th and 95th percentile bounds of posterior discrepancy. Third column: 5th and 95th percentile bounds of system prediction (black) and experimental data (blue). 51
Figure 19. Posterior mean δ response as a function of material distribution..... 52
Figure 20. Posterior mean surface of the system prediction (left) and 2D load-displacement (right) 53

Figure 21. (a) x vs θ4 scatter plot of the 131 simulation training data design, where the red points are the input settings excluded from Training Plan 2. (b) The 131 simulation training data where the runs marked in red are excluded for training plan 2 54
Figure 22. Posterior MCMC realizations of calibration inputs for Training Plan 2 55
Figure 23. Surrogate model hold-out residuals for Training Plan 2 56
Figure 24. (a) 5^{th} and 95^{th} percentile bounds for surrogate model responses using Training Plan 1 (black) and Training Plan 2 (green) for the 27%, 37%, 47%, 57%, and 67% nylon (b) 5^{th} and 95^{th} percentile bounds for system predictions using Training Plan 1 (black) and Training Plan 2 (green) for the 27%, 37%, 47%, 57%, and 67% nylon 58
Figure 25. Posterior mean δ response as a function of material distribution 60
Figure 26. Posterior mean surfaces of calibrated surrogate model (left) and system prediction (right) 61

List of Tables

Table 1. Notation for variable and calibration inputs 30
Table 2. Upper and lower bounds of calibration inputs 31
Table 3. Mean and variance of calibration parameters. For θ_1, the first and second entry correspond to the mean and variance of the smaller peak (low range) and larger peak (high range), respectively. 46
Table 4. Absolute residuals and RMSE of system predictions using calibrated $\boldsymbol{\theta}$ 48
Table 5. Absolute residuals and RMSE of system predictions using $\boldsymbol{\theta}$ from single material uniaxial testing 49
Table 6. The uncertainty bounds of the surrogate model responses for using 27%, 37%, 47%, 57%, and 67% nylon Training Plan 1 and Training Plan 2 59
Table 7 The uncertainty bounds of the system predictions for using 27%, 37%, 47%, 57%, and 67% nylon Training Plan 1 and Training Plan 2 59

Chapter 1: Introduction

The advent of additive manufacturing has unlocked many possibilities in rapid prototyping and printing complex geometries that are difficult to achieve with conventional manufacturing techniques [1]–[3]. Specifically, multi-material additive manufacturing allows the ability to control material property at a voxel level by creating a mesoscale material pattern [4]–[8]. This mesoscale design can offer macroscopically heterogeneous material properties. This differs from other efforts focusing more on statistically homogeneous systems, where materials are mixed randomly, or repeating unit cells of monolithic material are fabricated [4]–[6], [9]. Mesoscale heterogeneous material systems can be found in natural materials such as bones, bamboos, and mollusk shells [4], [10]–[16].

This design has shown adaptability in complex mechanical environments as can be found in functionally graded materials [17]–[20]. Mesoscale design, despite its potential, also poses the question of computational design optimization. Although microstructure optimization and topology optimization have been well explored, this intermediate field of mesostructure optimization still requires more attention [4], [7]. Mesostructure design consists of two parts: the forward problem of accurate prediction and inverse problem of efficient search, as shown in Figure 1. Here, we focus on the forward problem of accurately predicting the physical response of a mesostructured material. Based on fundamental mechanics laws, FEA assisted simulations can be conducted in order to model the material responses. However, this approach can be proven insufficient because of various computational uncertainties including the constituent material properties [4], [21], [22].

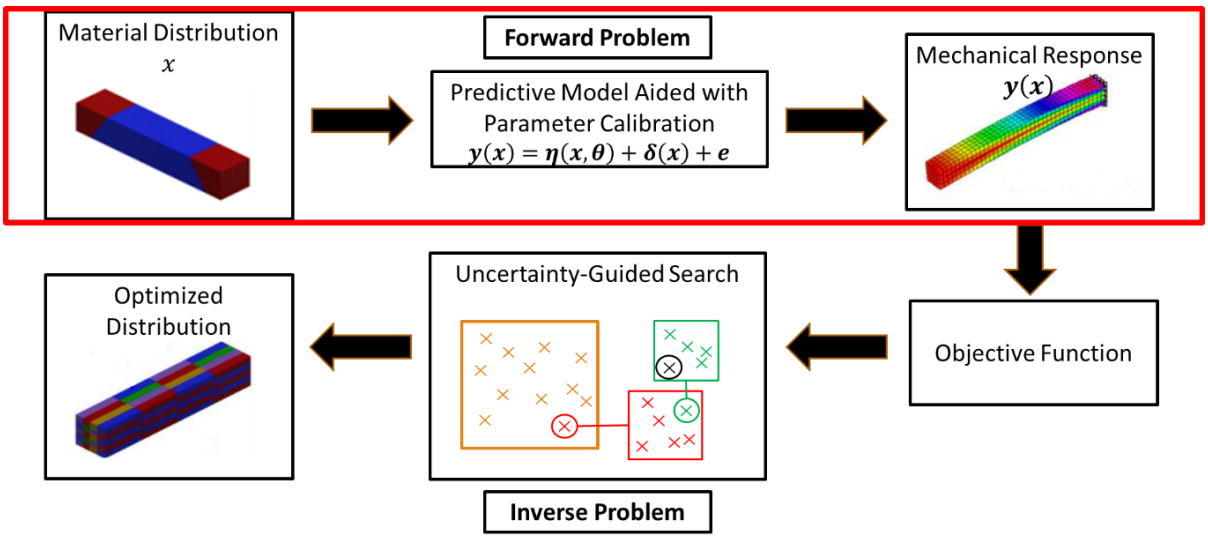

Figure 1. Forward and inverse problems of multi-material mechanical design. The highlighted portion is the focus of this thesis

We employ a Bayesian calibration method to calibrate our model, which entails statistically modeling the mechanical behavior by integrating both physical experiments and simulations [21], [23]. This calibration framework has been applied to a problem involving a mesostructure fabricated by fused deposition modeling. A constitutive model is developed to predict the three-point bend results of the mesostructure consisting of nylon and thermoplastic polyurethane (TPU). The material parameter values for this model are not sufficiently defined by exclusively using experimental procedures. We show that the implementation of a Bayesian calibration framework can account for the many model uncertainties and quantify this uncertainty for the calibrated material parameters. Additionally, fast and accurate predictions of the simulation and experimental output can be achieved by the integrated surrogate model and discrepancy term, while significantly reducing computational load.

Chapter 2: Literature Review

2.1 Mesoscale Heterogeneous Material Systems

Mesoscale materials refer to a materials system consisting of different material domains allowing for spatial variation in property at the length scale $0.1 - 1\text{mm}$. Previous efforts in mesostructure design were based in statistically homogeneous material systems such as randomly mixed mesoscale materials or architecture created by repeated unit cells [4]–[6]. Additionally, it is possible to create a mesostructured material with a single material but with varied macrostructures [4], [24]. Statistically homogeneous mesoscale materials consist of domains that are designed to be larger than molecular dimensions but smaller than the macroscopic length scale, meaning that the system can be considered homogeneous with an effective property [4]–[6].

However, a different focus point would be controlling the distribution of material within the structure to produce macroscopically inhomogeneous properties. This mesostructured design can allow for increased adaptability to various mechanical environments. Mesoscale heterogeneous material design aided by multi-material additive manufacturing is capable of controlling material distribution throughout the whole geometry space allowing for material property control at the voxel level, whereas the design space is limited for statistically homogeneous material systems [4]–[6]. Details on the capabilities of additive manufacturing will be further explored in Section 2.1. Another benefit of this material design is its adaptability to engineering applications that generally involve nonuniform stress fields due to complex loading conditions and other environmental factors. Given the capability of designating material properties in the necessary areas, the stress fields can be redistributed, which can improve the local stress concentration resistance, and overall load-bearing capacity [4], [7]. Natural examples of mesostructured heterogeneous materials include bamboos, bone, and mollusk shells [4], [10]–[12].

Common examples of mesostructured system within engineering are functionally graded materials. Functionally graded materials involve a gradual change in composition and structure over volume, where it is possible to create a material with a gradient of two compositions going from one to another [17]–[20]. In particular, metal-ceramic functionally graded materials have shown desirable properties in each component. The constituent ceramic can provide corrosion and oxidation protection for the metal as well as thermal barrier effects Toughening and strengthening properties can be given by the metal component [18], [19]. Additionally, the gradient interface between the

two components allows for reduction in thermal residual stresses. The presence of the gradient interface also shows decrease in the crack growth driving force [19].

With multi-material additive manufacturing enabling mesoscale design, possibilities in computational optimization are unlocked. Theoretical work investigating the effects of mesoscale design in a functionally graded cylinder aimed to reduce failure probability given Hertzian contact and a thin plate by Yu *et al.* [7] has demonstrated improvement in material usage, weight, and load bearing capacity. Further work in developing the framework of combining simulation data and physical observations for the bend resistance optimization of a mesostructured beam was done by Garcia *et al.* [4].

2.2 Multi-Material Additive Manufacturing

As mentioned in Section 2.1, advancements in multi-material additive manufacturing techniques has allowed for the fabrication of mesoscale materials. Additive manufacturing (AM) is an automated process which fabricates a 3-diemnsional part by adding material layer-by-layer onto previously deposited material. The process can also be described as rapid prototyping and 3D printing [1], [2]. Given a 3D Computer-Aided Design (CAD) model, AM enables the printing of complex geometries as well as increased freedom in design space [1], [2], [25]. Since the advent of AM, the various processes can generally be categorized as: laser-based, extrusion-based, and material jetting approaches [25].

Laser-based AM processes involve using a laser source with varying degrees of power to create the desired structure. These methods can also be divided by laser polymerization and laser melting processes. Laser polymerization methods generally consist of using a low-power laser source on a photosensitive resin. Stereolithography (SLA) is a representative example of laser polymerization where a thin layer of liquid resin on the built platform is solidified by photopolymerization when in contact with the UV laser. With laser melting processes such as laser engineering net shaping (LENS) and selective laser sintering (SLS), the laser source is used to melt or sinter material powder to solidify each layer of the structure [1], [2], [25].

Extrusion processes which are similar to conventional polymer extrusion processes involve a nozzle that is commonly heated to melt or soften the material which can be deposited at a constant flow rate onto the platform creating each layer. Well known technologies based on extrusion are

fused deposition modeling (FDM) and robocasting [1]–[3], [25], [26]. Material jetting which can also be denoted as 3D inkjet printing, describes the process where a print head is used to deposit a binder onto a powder bed. The solidification of the material is accomplished by a UV source at each pass [1], [2], [25].

The use of multi-material additive manufacturing to fabricate mesoscale heterogeneous materials has been demonstrated in polymers and metals through processes such as 3D inkjet printing, FDM, and LENS [4], [27], [28]. Fabrication of structures with gradient mechanical properties allowing for variation in local mechanical behavior has been accomplished for polyurethanes with the use of inkjet printing [27]. LENS involves the use of a high-powered laser to melt metal powder to deposit each material layer. The powder is fed through a delivery nozzle usually by a carrier gas [1], [2], [25]. Gradient material distribution can also be achieved with LENS by controlling the flow rate of powder delivery [28]–[30]. An example involves a gradient $\mathrm{Ti} - \mathrm{TiO_2}$ material with a top surface of 50% $\mathrm{TiO_2}$ led to increased surface wettability and hardness allowing for a reduced rate of wear [4], [30]. LENS processes can also be used to create material systems with discrete material voxels with a specific type of material and has been demonstrated with SS316 and IN625 alloys [4], [31].

For our problem, we focused on the use of FDM to create the mesoscale heterogeneous material systems with discrete material boundaries. Multi-nozzle extrusion processes have been used to create layered tissue scaffolds consisting of a poly (L-lactic acid) composite with varying porosity and concentration of bone morphogenic protein [32]. Another example also demonstrated extrusion processes used to fabricate a patterned hydrogel with varied material properties and control of local stiffness [26].

2.3 Constitutive Modeling and Simulations

The applied pattern of varied material properties in a mesostructure means that the mechanical behavior will reflect this material distribution. To investigate how these material properties can affect the mechanical behavior of a mesostructured material through simulations, finite element analysis (FEA) can be used, as long as the fundamental mechanics law for each constituent material is known.

FEA is a widely used numerical method aimed to solve partial differential equations for a variety of engineering problems. The material can be represented as a finite element mesh where the geometry is discretized by interconnected nodes. Node which carry unknown variables denoted as field variables are to be computed during FEA. The non-nodal variables are approximated using interpolation functions or shape functions using values of the field variables. A solution can be approximated by then applying boundary conditions to the model and solving the finite element equations [33], [34]. Models created to simulate the mechanical properties of mesoscale heterogeneous materials and parts fabricated via AM have been previously explored [4], [7], [22], [35].

A model of a multi-layered material consisting of metallic and composite plies has been developed by Coutellier and Rozycki [35]. Here, the metallic ply was defined to exhibit elastic plastic behavior and two different methods were used to describe the composite ply. The first used a bi-phase model which treats the mechanical behavior of the constituent fibers and matrix separately, while the second method defines the composite as a homogeneous layer. In Xu *et al*. [36], FEA is utilized to predict effective material properties of a heterogeneous material consisting of discrete epoxy and glass domains in a two-dimensional plane strain configuration. The two materials were selected based on the large difference in elastic properties. Additionally, investigation into mechanical properties with cellular lattice parts printed by fused deposition modeling has been conducted by Ravari *et al*. [22]. The structure was modeled as either beam or solid elements with material parameters based on bulk compression tests.

Despite insights that can be gained from FEA, the computational load of these simulations has become an obstacle during model development as more detailed and accurate geometries tend to lack computational efficiency [21], [22]. For example, when modeling cellular lattice structures, solid models were found to be much more accurate compared to the beam model but required a higher computational cost [22]. So, despite efforts in increasing computational efficiency within the computational scheme itself, it introduces a significant amount of uncertainty in the model output. In this thesis, we looked to circumvent the issue of computational cost by implementing a statistical representation of our computer model and calibrate it through techniques based in Bayesian inference.

2.4 Computer Model Uncertainty and Model Calibration

As discussed previously in Section 2.3, uncertainty can be introduced in a FEA model based on modeling choices. Several sources of computer model uncertainty can be identified, as shown by Kennedy and O'Hagan [21], that we aim to accomodate for by means of Bayesian calibration.

A very important focus of this thesis concerns the parameter uncertainty of the computer model. The parameters derived from physical experiments may not match the true value. In our problem, these unknowns are the constituent material properties of the mesostructure, and their uncertainty will be described further in Section 3.3. Calibration can provide insight on the true values of our unknown parameters.

Another major source of uncertainty is with model discrepancy, which refers to the inadequacy present in the computer model output when compared to physical experiments. This can be attributed to imperfect understanding of the physics and other approximations introduced during the modeling process. Although our FEA model formulation is meant to output the same results given repeated simulations with the same input settings, this may not always be the case in other applications, bringing in some residual variability.

Previous efforts in model calibration have mostly centered around addressing the problem of parameter uncertainty [37]–[42]. Desai and Chen [38] employ numerical methods of quasi-Newton optimization to calibrate disturbed state concept (DSC) constitutive models. Although this parameter calibration scheme can improve the predictive capabilities of the constitutive model, it does not answer the problem of model inadequacy and high computational cost.

Fireworks optimization algorithm (FWA) has been utilized by Karkalos and Markopoulos [40], in determining the Johnson-Cook material parameters for AISI 316L stainless steel. FWA is categorized under Swarm Intelligence (SI) methods and involves searching a large solution space by dispersing random points to search for the optimal solution.

For masonry constitutive models, the unknown parameter values were found using genetic algorithms, which is a machine learning method based in evolutionary process theory [37], [42]. A surrogate model formulated by moving least squares (MLS) approximation was used to estimate the least square difference between the experimental and simulation output. The genetic algorithm

optimization is based on minimizing the surrogate model response. This method can be used to model highly noisy data but does not accommodate for model uncertainty.

2.5 Local Deformation Characterization via Digital Image Correlation

The local mechanical behavior of a mesostructured material can be closely observed by digital image correlation (DIC). The DIC technique is an effect method for characterizing an array of mechanical responses. For our problem, DIC can be used to characterize the local deformation of the surface material voxels, providing full-field displacements and strain maps [4], [43]–[47]. DIC methods are based in conventional digital photography making it more advantageous than optical techniques including interferometric methods and laser shearography, which involves larger costs and more precise experimental setups [44], [46]. Interferometric techniques generally require low vibration-isolated environments and a coherent light source [46]. DIC methodology is based in digital image processing and numerical techniques, where images of the deformed surface is taken and using a predefined criterion and optimization algorithm, the images are compared to the reference or undeformed material surface [46]–[48].

The DIC imaging process requires the material surface to have a random gray intensity distribution or speckle pattern [46], [47]. After defining the reference image, the surface is split into evenly spaced grids, where each node is used to calculate the full-field deformation [46]. These grid points are tracked during the measurement process where, as previously mentioned, the reference and deformed images are compared to compute the displacement. At a certain point, for the reference, a square reference subset of surrounding pixels is selected for comparing the gray intensity between the two states. These subsets allow for an easier identification of deformation through gray intensity comparison than when using individual pixels [46]–[48].

The differences between the reference and deformed state can be computed by a predefined criterion such as, a cross-correlation criterion or the sum-squared difference correlation criterion. Previous work by Pan *et al*. [49] has shown that zero-mean normalized sum of squared difference criterion and zero-mean cross correlation criterion improved accuracy in the comparisons since it does not account for changes in scale and offset changes of the deformed state gray intensity [47]. The measurement accuracy can be increased by implementing different subpixel displacement measurement algorithm [46].

Although DIC techniques show relatively higher ease of use with its flexibility in experimental setups, there are still some errors that can be introduced. A common source of error is from the random noise that can be captured during the imaging process. Additionally, the quality of speckling, which can vary sample to sample due to randomness, has a large effect on the measurement accuracy. These disadvantages can lead to an overall accuracy lower than interferometric methods [46]–[48]. Recent studies by Yong *et al*. [48] investigated the modeling of the spatial uncertainty attributed to the random speckling. Despite these disadvantages of DIC, it is still an effective way to compare the local deformation behavior between a single material design and a mesoscale heterogeneous material design [4].

2.6 Overview of Bayesian Inference

With the aim of material parameter calibration, we apply Bayesian calibration approaches closely following that of Higdon *et al*. [23] and Kennedy and O'Hagan [21]. Before reviewing the details of our methodology, it is important to introduce basics of Bayesian inference. Bayesian methods involve specifying a prior distribution which includes prior information or beliefs about unknowns of a given process and updating this prior by a sampling model or likelihood which contains information of the observed data or training data. This updating gives a posterior distribution which is a conditional distribution of the unknowns given the observed data and realizations can be drawn from these posterior distributions [50], [51].

This process can be mathematically expressed through the Bayes theorem. Given the observed data $\boldsymbol{y} = y_1, \dots, y_n$, we want to be able to learn more about a specific physical process by its random unknown parameters $\boldsymbol{\theta}$. The posterior probability distribution of the parameter $\boldsymbol{\theta}$ conditional on the observations are denoted as $\pi(\boldsymbol{\theta}|\boldsymbol{y})$. The mathematical expression for obtaining this term can be written as

$$\pi(\boldsymbol{\theta}|\boldsymbol{y}) = \frac{\pi(\boldsymbol{\theta}, \boldsymbol{y})}{\pi(\boldsymbol{y})} = \frac{L(\boldsymbol{y}|\boldsymbol{\theta})\pi(\boldsymbol{\theta})}{\int L(\boldsymbol{y}|\boldsymbol{\theta})\pi(\boldsymbol{\theta})\mathrm{d}\theta}, \tag{1}$$

where the likelihood or sampling model is denoted as $L(\boldsymbol{y}|\boldsymbol{\theta})$ and the prior is $\pi(\boldsymbol{\theta})$. Posterior realizations of each parameter of interest can be taken by MCMC sampling methods on the full conditional distributions for $\pi(\boldsymbol{\theta}|\boldsymbol{y})$. The normalization term $\int L(\boldsymbol{y}|\boldsymbol{\theta})\pi(\boldsymbol{\theta})\mathrm{d}\theta$ can be ignored when sampling [50], [51].

A simple example involves learning parameters μ and λ_y given observed data y where

$$y(x_i) = \mu + \varepsilon_i, \;\; \varepsilon_i \sim N\left(0, \lambda_y^{-1}\right), \;\; i = 1, \ldots, n. \tag{2}$$

The sampling model for the data conditional on the parameters μ and λ_y can be written as

$$L\left(y|\mu, \lambda_y\right) \propto \prod_{i=1}^{n} \lambda_y^{\frac{1}{2}} \exp\left[-\frac{1}{2}\lambda_y (y_i - \mu)^2\right]. \tag{3}$$

The prior distributions can be specified as

$$\pi(\mu) \propto 1; \tag{4}$$

$$\pi\left(\lambda_y\right) \propto \Gamma\left(a_y, b_y\right). \tag{5}$$

Following Bayes rule, the posterior distribution can be computed through

$$\begin{aligned} \pi\left(\mu, \lambda_y|y\right) &\propto L\left(y|\mu, \lambda_y\right) \times \pi(\mu) \times \pi(\lambda_y) \\ &\propto \lambda_y^{\frac{n}{2}} \exp\left[-\frac{1}{2}\lambda_y \sum_{i=1}^{n} (y_i - \mu)^2\right] \times \lambda_y^{a_y - 1} \exp\left[-b_y \lambda_y\right]. \end{aligned} \tag{6}$$

Each parameter can be explored by alternately sampling from their full conditional distributions.

$$\pi\left(\mu|y, \lambda_y\right) \propto \exp\left[-\frac{1}{2}\lambda_y \sum_{i=1}^{n} (y_i - \mu)^2\right]; \tag{7}$$

$$\pi\left(\lambda_y|y, \mu\right) \propto \lambda_y^{a_y + \frac{n}{2} - 1} \exp\left[b_y + \frac{1}{2}\sum_{i=1}^{n} (y_i - \mu)^2\right]. \tag{8}$$

2.7 Overview of Gaussian Process

A thorough understanding of the computer simulation output is necessary for comprehensive uncertainty analysis or sensitivity analysis [21]. However, this type of analysis is limited by large computational loads. Given that a computer model produces output that varies smoothly as a function of the inputs, it is possible to use a smaller sample of simulations to model the response

[21], [52]–[54]. In this paper, the Gaussian Process (GP) is used as a statistical representation for the simulator output. This section will serve as a brief overview of GPs.

GPs can be defined as for any subset of $i = 1, \dots, n$ where $x_1, \dots, x_n \in \chi$, the joint distribution of $f(x_1), \dots, f(x_n)$ will be multivariate normal. These distributions can be described by their mean function $m(\cdot)$ and covariance function $c(\cdot,\ \cdot)$. GPs are commonly used for their convenience and realistic properties within statistics and modeling [52]–[55].

$$f(\cdot) \sim \mathrm{GP}\big(m(\cdot), c(\cdot,\cdot)\big). \tag{9}$$

For example, if the process was restricted to a single point x, the distribution can be defined as

$$f(x) \sim N\big(m(x), c(x,x')\big). \tag{10}$$

The GP is used to fit the simulator Modeling the simulator is can be done by a stationary GP for computer models with reasonably smooth output. Stationarity refers to the mean remaining constant and the covariance being a function of $\mathbf{x} - \mathbf{x}'$. Since the covariance function comes from a multivariate normal distribution, the variance-covariance matrix of $f(x_1), \dots, f(x_n)$ needs to be non-negative definite for all $\mathbf{x_i} \in \chi$. The covariance function should also exhibit properties of an even function due to its symmetry.

$$c(x,x') = E\big[\big(f(x) - \mathrm{m}(x)\big)\big(f(x') - \mathrm{m}(x')\big)\big] = c(x',x). \tag{11}$$

The main importance of $c(\cdot,\cdot)$ lies in that it models the correlation between $f(\mathbf{x})$ and $f(\mathbf{x}')$. Where if x and x' are similar in χ, then $f(x)$ and $f(x')$ will be similar as well. This indicates a reasonable assumption that $f(\cdot)$ will be smooth.

As mentioned previously, a GP can be described entirely by its mean and covariance. This information can be used to then draw random samples from the GP. In the multivariate normal case of $\mathbf{x_i} \in \chi$, there will be mean and covariance functions $m(\cdot)$ and $c(\cdot,\cdot)$ where samples can be generated from [54]. First the covariance matrix must be computed for the points of interest:

$$c_{ij} = c\big(x_i, x_j\big). \tag{12}$$

Then the Cholesky decomposition of the matrix is computed to result in L:

$$\mathrm{C} = LL^T. \tag{13}$$

Using specified mean and standard normal samples, u, we can write a vector z that can be sampled [54], [56]:

$$z = m + Lu. \tag{14}$$

The covariance function $c(\cdot,\cdot)$ can be modeled hierarchically [21], [52]–[55].

$$c(x, x') = \sigma^2 * r(x, x'; \omega). \tag{15}$$

Where $r(\cdot,\cdot)$ refers to the correlation function, and variance σ^2 is the scaling parameter that can control how far the model response will stray from the mean. The extension of the correlation function can be controlled with its hyperparameters. The following is the formulation of a power exponential correlation function which is a flexible choice for a correlation function [21], [23].

$$r(x, x') = \exp\left[-\sum_{j=1}^{q} \beta_j \left(x_j - x_j'\right)^{\alpha_j}\right]. \tag{16}$$

This form allows for a smooth representation for GP models when α is near 2. The β_j's control the dependence strength and thus the sensitivity of the GP model response for each input. The α_j's can determine the smoothness of the model response. Prior distributions for variance σ^2 and parameters $\beta_1, .., \beta_j$ and $\alpha_1, ..., \alpha_j$ can be specified.

2.8 Gaussian Process Surrogate Model

As discussed previously, to circumvent issues that come with the high computational cost of computer models, GPs can be used to formulate a statistical model of the simulator output, which can be denoted as the surrogate model. GPs are a favorable choice for a surrogate model because it meets the criteria of interpolating the given data points completely, while providing a providing distribution at unknown points to represent the uncertainty [21], [52]–[54].

We can now have a more detailed look at the GP surrogate model formulation. Given data from the complex computer simulator, $\boldsymbol{y} = (y_1, \dots, y_n)$ at input settings $\boldsymbol{s} = (s_1, \dots, s_n)$, the output can be modeled as

$$y(\boldsymbol{s}) = z + \epsilon, \quad \epsilon \sim N\left(0, \frac{1}{\lambda_y} I_n\right), \tag{17}$$

where the data $\boldsymbol{y}$ is defined as a noisy observation of $\boldsymbol{z}$. The trained GP model is intended to estimate the simulator response by drawing realizations of $\boldsymbol{z}$. This is accomplished by formulating a posterior probability distribution of the relevant parameters conditional on the data, from which samples can be drawn. From here, the sampled parameters can be used to obtain z predictions. So, the formulation of a GP surrogate model follows Bayesian inference rules [57]–[60].

The prior for $z(s)$ is described as a 0 mean GP defined by the power exponential covariance applied to each input setting $\boldsymbol{s}$.

$$c(\boldsymbol{s}, \boldsymbol{s}') = \frac{1}{\lambda_z} \exp[-\beta(\boldsymbol{s} - \boldsymbol{s}')^2]. \tag{18}$$

For the sake of convenience, it is possible to express the spatial dependence parameter β as

$$\beta = -4 \log(\rho). \tag{19}$$

The covariance term can now be written as

$$c(\boldsymbol{s}, \boldsymbol{s}') = \frac{1}{\lambda_z} R\big((\boldsymbol{s}, \boldsymbol{s}'); \rho\big), \quad R = \rho^{4(\boldsymbol{s} - \boldsymbol{s}')^2}. \tag{20}$$

Gamma priors can be specified for the hyperparameter λ_z and λ_y, and a Beta prior can be specified for ρ.

$$\pi(\lambda_z) \propto \lambda_z^{a_z - 1} \operatorname{Exp}[-b_z \lambda_z]; \tag{21}$$

$$\pi\big(\lambda_y\big) \propto \lambda_y^{a_y - 1} \operatorname{Exp}\big[-b_y \lambda_y\big]; \tag{22}$$

$$\pi(\rho) \propto \rho^{a_\rho - 1}(1 - \rho)^{b - 1}. \tag{23}$$

The likelihood of the data given $\boldsymbol{z}$ can be expressed as well as a joint likelihood of both the data and $\boldsymbol{z}$ conditional on the hyperparameters by introducing the prior term for $\boldsymbol{z}$:

$$L(\boldsymbol{y}|\boldsymbol{z},\lambda_y) \propto \lambda_y^{\frac{n}{2}} \exp\left[-\frac{1}{2}\lambda_y(\boldsymbol{y}-\boldsymbol{z})^{\mathrm{T}}(\boldsymbol{y}-\mathbf{z})\right]; \tag{24}$$

$$\begin{aligned} L(\boldsymbol{y},\boldsymbol{z}|\lambda_y,\lambda_z,\rho) \propto \lambda_y^{\frac{n}{2}} \exp\left[-\frac{1}{2}\lambda_y(\boldsymbol{y}-\boldsymbol{z})^{\mathrm{T}}(\boldsymbol{y}-\mathbf{z})\right] \\ \times \lambda_z^{\frac{n}{2}}|R(\rho;s)|^{-\frac{1}{2}} \operatorname{Exp}\left[-\frac{1}{2}\lambda_z z^{\mathrm{T}} R(\rho;\mathrm{s})^{-1} z\right]. \end{aligned} \tag{25}$$

Since realizations of the parameters need to be obtained before being able to make predictions of $\boldsymbol{z}$, the $\boldsymbol{z}$ term is marginalized out.

$$\begin{aligned} L(\boldsymbol{y}|\lambda_y,\lambda_z,\rho) \propto \left|\frac{1}{\lambda_y} I_n + \frac{1}{\lambda_z} R\big((\boldsymbol{s},\boldsymbol{s}');\rho\big)\right|^{-\frac{1}{2}} \\ \operatorname{Exp}\left[-\frac{1}{2} y^{\mathrm{T}} \left(\frac{1}{\lambda_y} I_n + \frac{1}{\lambda_z} R\big((\boldsymbol{s},\boldsymbol{s}');\rho\big)\right)^{-1} y\right]. \end{aligned} \tag{26}$$

The posterior for the parameters of interest conditional on the data can now be found by combining the priors and marginal likelihood.

$$\begin{aligned} \pi(\lambda_y,\lambda_z,\rho|y) \propto L(\boldsymbol{y}|\lambda_y,\lambda_z,\rho) \times \pi(\lambda_z) \times \pi(\lambda_y) \times \pi(\rho) \\ \propto \left|\frac{1}{\lambda_y} I_n + \frac{1}{\lambda_z} R\big((\boldsymbol{s},\boldsymbol{s}');\rho\big)\right|^{-\frac{1}{2}} \operatorname{Exp}\left[-\frac{1}{2} y^{\mathrm{T}} \left(\frac{1}{\lambda_y} I_n + \frac{1}{\lambda_z} R\big((\boldsymbol{s},\boldsymbol{s}');\rho\big)\right)^{-1} y\right] \times \lambda_z^{a_z-1} \operatorname{Exp}[-b_z\lambda_z] \\ \times \lambda_y^{a_y-1} \operatorname{Exp}\big[-b_y\lambda_y\big] \times \rho^{a_\rho-1}(1-\rho)^{b-1}. \end{aligned} \tag{27}$$

Metropolis sampling methods can be used to draw realizations from the posterior, which will be discussed further in Section 2.10. Using these samples of $(\lambda_y,\lambda_z,\rho)$, a joint distribution for (z,z^*) can be formulated to make m predictions of z^* [61].

$$\begin{aligned} \begin{pmatrix} z \\ z^* \end{pmatrix} \Big| \ldots \Big) \sim N\left(\begin{pmatrix} 0_n \\ 0_m \end{pmatrix}, \begin{pmatrix} \lambda_y^{-1} I_n + \Sigma_{z,z} & \Sigma_{z,z^*} \\ \Sigma_{z^*,z} & \Sigma_{z^*,z^*} \end{pmatrix}\right); \\ \Sigma_{z,z^*} = \lambda_z^{-1} R\big((\boldsymbol{s},\boldsymbol{s}^*);\rho\big). \end{aligned} \tag{28}$$

Conditional normal rules can be applied to the joint distribution to generate samples of z^* predictions.

$$(z^*|z) \sim N\left(\Sigma_{z^*,z}\left(\lambda_y^{-1} I_n + \Sigma_{z,z}\right)^{-1} z, \Sigma_{z^*,z^*} - \Sigma_{z^*,z}\left(\lambda_y^{-1} I_n + \Sigma_{z,z}\right)^{-1} \Sigma_{z,z^*}\right). \quad (29)$$

2.9 Singular Value Decomposition

Principal component analysis (PCA) aims to reduce the dimensionality of a multivariate variable **x** by analyzing its variances. It is an orthogonal transformation that projects the variables into a lower dimensional space, meaning a subset of variables will be selected. Principal components (PCs) are the dimensions or directions that displays the largest variances among the multivariate variable, where the first PC should account for the largest variance [55], [62], [63]. In addition to the use of GP surrogate models, we apply the use of principal components to further reduce the computational load during the calibration [23], [64].

Singular value decomposition (SVD) is another method that can be used to obtain these PCs. Given a $m \times n$ matrix **A**, according to SVD it can be decomposed as

$$\mathbf{A} = \mathbf{USV}^{\mathrm{T}}. \quad (30)$$

Where **U** and **V** are matrices of singular columns u_i and singular rows v_i, where these components are orthogonal basis functions. Matrix **S** consists of non-zero singular values s_i which decrease monotonically. The v_i entries describe the principal component directions which contain the directions of maximal variance for which the data points will be projected along. The $u_i s_i$'s are the principal component scores which represent the projections [62], [63].

It is possible to represent $\mathbf{Z} = \mathbf{US}$, allowing the original matrix values to be expressed as a linear combination

$$x_{ij} = \sum_{k=1}^{r} z_{ik} v_{ik}. \quad (31)$$

2.10 Basis Representation

Given data points $y_1, \dots, y_n$, a possible method of determining the appropriate $f(\cdot)$ by specifying a set of basis functions $b_1, \dots, b_m$ and coefficients $w_1, \dots, w_m$ to represent the function as a linear combination [23], [64], [65].

Basis representation can be applied when formulating a surrogate model for the simulator. As previously discussed, the given simulator can be represented as a function $f(\cdot)$ mapping inputs $\boldsymbol{x}$ to output space $\boldsymbol{y}$ [23]. Using the principal components $\boldsymbol{K}$, it is possible to project to the basis transformed space $\boldsymbol{y}^{PC}$. With the use of GPs and basis representation, the computational load of mapping the inputs $\boldsymbol{x}$ to the output space $\boldsymbol{y}$ is significantly reduced. So, the function can be represented as the linear combination of GP $w_i(\cdot), i = 1, \dots, m$

$$y(\cdot) = f(\cdot) = \sum_{i=1}^{m} w_i b_i. \tag{32}$$

where the formulation of basis coefficients $\boldsymbol{w}$ will be specified in Section 3.4.1.

2.11 Markov Chain Monte Carlo Methods

Markov Chain Monte Carlo (MCMC) is described as a class of algorithms that can be applied within Bayesian inference to draw realizations from complicated probability distributions. MCMC methods are useful because it allows for sampling a distribution with limited understanding of the mathematical properties of the probability distribution. MCMC consists of principles of Markov chains and the Monte Carlo method [66]–[70].

Markov chains refer to a stochastic sequential random sampling process, where the future samples only depend on the current sample, but it will be independent of the past samples. With the goal of sampling a stochastic process x_i from the target distribution $p(x)$, the x_i can be defined as a Markov chain [69], [70].

$$p(x_i|x_{i-1}, \dots x_1) = p(x_i|x_{i-1}). \tag{33}$$

In the context of x_i only taking on discrete values within a finite state space, a transition matrix T can be specified to change the probability of each state after each iteration. After sufficient

iterations, the probabilities are expected to converge, which is an important property within MCMC where the Markov chain is meant to converge at the target distribution. To satisfy this, the transition matrix T will need to have properties of irreducibility and aperiodicity [67]–[71]. Aperiodicity allows the chain to not get trapped in cycles, and irreducibility makes it so that there is positive probability of visiting another state given any state. These properties can be translated to the continuous state space by defining the transition matrix T as a transition kernel $T(x_{i+1}|x_i)$, where the mathematical representation is,

$$\int p(x_i)T(x_{i+1}|x_i). \tag{34}$$

Monte Carlo is a type of simulation method that can be used to estimate a probability distribution. Calculating the expected value of this density would require the computation of the integral:

$$\mathrm{E}[X] = \int x \cdot f(x)dx. \tag{35}$$

Instead of computing this integral, the Monte Carlo method involves drawing N random realizations of x from the target density $p(x)$ to approximate the density, which can be mathematically calculated as:

$$I_N = \frac{1}{N}\sum_{i=1} x_i \approx \int x \cdot f(x)dx. \tag{36}$$

As previously mentioned, the combination of the principles of Markov chains and Monte Carlo can allow for sampling from a distribution that cannot be done directly. This involves constructing the Markov chain using the given algorithm to be used to approximate the target distribution. A straightforward approach to accomplishing this is through the Gibbs sampler [67], [71].

Given a set of parameters of interest $\boldsymbol{\theta} = (\theta_1, \dots, \theta_n)$, a joint distribution $\pi(\boldsymbol{\theta})$ can be defined. Additionally, the full conditional distributions can be expressed as $\pi(\theta_i|\theta_{-i})$ for each θ_i conditional on the rest of the θ's. The first step involves initializing the parameters at set values $\boldsymbol{\theta}^0 = (\theta_1^0, \dots, \theta_n^0)$. From here, random samples from full conditional distributions $\pi(\theta_i|\theta_{-i}), i = 1, .., n$ can be drawn.

draw θ_1^1 from $\pi(\theta_1|\theta_{-1}^0)$

draw θ_2^1 from $\pi(\theta_1|\theta_1^1, \theta_3^0, \dots, \theta_n^0)$

$\vdots$

θ_n^1 from $\pi(\theta_n|\theta_{-n}^1)$.

As shown, the parameters are sampled consecutively so that the θ_i^j sample is conditioned on the previously drawn θ_{i-1}^j. This would be a full iteration of the Gibbs sampler and after t iterations, it will produce the Markov chain $\theta^0, \theta^1, \dots, \theta^t$. This Markov chain of realizations is expected to represent the joint distribution of all the parameters, where a single subset θ_i would be the marginal distribution.

Another example of an MCMC algorithm is Metropolis sampling. This approach shares similarities with the Gibbs sampler with its initialization and consecutive updating, but the key difference is that each sample is accepted based on the acceptance ratio [50], [68].

The process is started by initializing the parameters of interest $\boldsymbol{\theta}^0 = (\theta_1^0, \dots, \theta_n^0)$. As with the Gibbs sampler, there is less interest in the initialized value of the parameters since the Markov chain is expected stabilize at the target distribution. At the current time step j, the non-normalized density $\pi(\theta_i^j|\theta_{-i})$ can be computed. At the new step $j+1$, a random sample θ_i^{j+1} from a symmetric proposal distribution $q(\theta_i^{j+1}|\theta_{-i})$ centered at the current parameter value is drawn and the density $\pi\left(\theta_i^{j+1}\middle|\theta_{-i}\right)$ can also be computed. The acceptance probability can be computed as:

$$\alpha = \min\left[1, \frac{\pi\left(\theta_i^{j+1}\middle|\theta_{-i}\right)}{\pi\left(\theta_i^{j}\middle|\theta_{-i}\right)}\right]. \tag{37}$$

The new sample will always be accepted if the acceptance probability $\alpha = 1$ meaning that the calculated. When $\alpha < 1$, the new sample θ_i^{j+1} is not automatically discarded, but a random sample from a uniform distribution is drawn. If the uniform sample is larger than α, then θ_i^{j+1} is discarded and the current sample θ_i^j is accepted.

The Metropolis sampling method is considered a modification of the Hastings procedure [50], [67], [72]. The first step of Hastings sampling also consists of initializing the parameters $\boldsymbol{\theta}^0 =$

$(\theta_1^0, \dots, \theta_n^0)$. The non-normalized density $\pi(\theta_i^j|\theta_{-i})$ at the current iteration j can be calculated. At iteration $j+1$, a new sample θ_i^{j+1} is sampled from a proposal distribution $q(\theta_i^{j+1}|\theta_{-i})$. The density with this new sample is calculated as $\pi\left(\theta_i^{j+1}\middle|\theta_{-i}\right)$. A proposal correction factor can be computed:

$$c = \frac{q\left(\theta_i^j\middle|\theta_{-i}\right)}{q\left(\theta_i^{j+1}\middle|\theta_{-i}\right)}. \tag{38}$$

The acceptance probability can now be calculated by:

$$\alpha = \min\left[1, \frac{\pi\left(\theta_i^{j+1}\middle|\theta_{-i}\right)}{\pi\left(\theta_i^j\middle|\theta_{-i}\right)} \times c\right]. \tag{39}$$

Sample acceptance follows the same rule where the new sample θ_i^{j+1} will be accepted when $\alpha = 1$. The current θ_i^j is accepted when $u > \alpha$, given a random number draw u from a uniform distribution. As discussed before, the histogram of these samples will give an approximation of the target distribution.

2.12 Univariate Model Formulation

This section will discuss the general univariate model formulation described by Kennedy and O'Hagan [21] and Higdon et al. [23]. The basis formulation applied to our problem will be detailed when discussing the experimental methods in later sections.

The physical observations $\boldsymbol{y} = (y_1, \dots, y_n)$ of an experiment at variable inputs $\boldsymbol{x} = (x_1, \dots, x_n)$ can be modeled by:

$$y(x_i) = \zeta(x_i) + \epsilon(x_i), i = 1, \dots, n. \tag{40}$$

The real physical response is denoted as $\zeta(x_i)$ and $\epsilon(x_i)$ is the observation error. In the context of our problem, the variable inputs x_i represent the materials distributions and index the applied loads, $\zeta(x_i)$ would represent the displacement of the material system. The model can integrate the

expression for the simulator $\eta(\boldsymbol{x}, \boldsymbol{\theta})$ at the optimal calibration input $\boldsymbol{\theta}$ as well as the discrepancy term $\delta(\boldsymbol{x})$.

$$y(x_i) = \eta(x_i, \theta) + \delta(x_i) + \epsilon(x_i), i = 1, \dots, n. \tag{41}$$

The discrepancy term $\delta(\boldsymbol{x})$ accounts for the inadequacies of the simulator $\eta(\boldsymbol{x}, \boldsymbol{\theta})$. The function of the discrepancy can vary based on the application and the functionality of the simulator. The unknown, optimal calibration input was expressed as $\boldsymbol{\theta}$ which is denoted as $\boldsymbol{t}$ for the calibration inputs used for running the simulator. The restriction to m simulation runs can be noted as:

$$\eta\left(x_j^*, \theta_j^*\right), j = 1, \dots, m. \tag{42}$$

From here we can apply a GP prior model as a surrogate model for $\eta(\boldsymbol{x}, \boldsymbol{\theta})$ to circumvent the large computational cost the simulator requires during the calibration process. The GP model requires the specification of a mean function $m(\boldsymbol{x}, \boldsymbol{t})$ and covariance function $\mathrm{Cov}((\boldsymbol{x}, \boldsymbol{t}), (\boldsymbol{x}', \boldsymbol{t}'))$, where the GP will be mean zero**.** The covariance function is specified with a power exponential form:

$$\begin{aligned} \mathrm{Cov}\left((\boldsymbol{x}, \boldsymbol{t}), (\boldsymbol{x}', \boldsymbol{t}')\right) &= \frac{1}{\lambda_\eta} \prod_{k=1}^{p_t} \rho_{\eta k}^{4\left(x_k - x_k'\right)^2} \times \prod_{k=1}^{p_t} \left(\rho_{\eta, p_x + k}\right)^{4\left(t_k - t_k'\right)^2} \\ &= \frac{1}{\lambda_\eta} R\left((\boldsymbol{x}, \boldsymbol{t}), (\boldsymbol{x}', \boldsymbol{t}'); \boldsymbol{\rho}_\eta\right). \end{aligned} \tag{43}$$

The marginal precision parameter for $\eta(\cdot, \cdot)$ is denoted as λ_η and spatial dependence parameter for each input x and t, is denoted as $\boldsymbol{\rho}_\eta$. $\rho_{\eta k}$ controls of the dependence of the GP model response with respect to each x_i. The smoothness parameter is specified as $\boldsymbol{\alpha} = 2$ to allow for the GP model representation to be smooth and infinitely differentiable. The prior is fully specified by defining priors $\pi(\mu), \pi\left(\lambda_\eta\right)$, and $\pi(\boldsymbol{\rho}_\eta)$ for the hyperparameters.

The discrepancy model $\delta(\boldsymbol{x})$ aims to account for the difference between physical observations and simulation output due to either incomplete physics or approximations during the development of the simulator model. The discrepancy model only depends on the variable input $\boldsymbol{x}$, and to effectively model the change in discrepancy over the range of inputs, the covariance function can be expressed as:

$$\begin{aligned}\mathrm{Cov}(\boldsymbol{x}, \boldsymbol{x}') &= \frac{1}{\lambda_\delta} \prod_{k=1}^{p_x} \rho_{\delta k}^{4(x_k - x_k')^2} \\ &= \frac{1}{\lambda_\delta} R((\boldsymbol{x}, \boldsymbol{x}'); \boldsymbol{\rho}_\delta.\end{aligned} \tag{44}$$

As with the GP model for the simulator, the hyperparameters will have prior distributions $\pi(\lambda_\delta)$ and $\pi(\boldsymbol{\rho}_\delta)$ specified as well.

With these prior specifications it is now possible to formulate the likelihood for the combined data D. The physical observations can be shown as the vector $\boldsymbol{y} = \big(y(x_1), \dots, y(x_n)\big)^T$ and the simulation output can be defined as $\boldsymbol{\eta} = \big(\eta(x_1^*, t_1^*), \dots, \eta(x_m^*, t_m^*)\big)^T$. With given variable inputs $(x_1, \boldsymbol{\theta}), \dots, (x_n, \boldsymbol{\theta})$ and calibration input settings $(x_1^*, t_1^*), \dots, (x_m^*, t_m^*)$, the combined data can be expressed as a $(n+m)$-vector $D = (\boldsymbol{y}^T, \boldsymbol{\eta}^T)^T$. The likelihood can then be defined as:

$$L\big(D \big| \boldsymbol{\theta}, \lambda_\eta, \lambda_\delta, \boldsymbol{\rho}_\eta, \boldsymbol{\rho}_\delta, \boldsymbol{\Sigma}_y\big) \propto |\boldsymbol{\Sigma}_D|^{-\frac{1}{2}} \operatorname{Exp}\left[-\frac{1}{2} D^T \boldsymbol{\Sigma}_D^{-1}\right]. \tag{45}$$

The covariance term $\boldsymbol{\Sigma}_D$ consists of:

$$\boldsymbol{\Sigma}_D = \boldsymbol{\Sigma}_\eta + \boldsymbol{\Sigma}_{\boldsymbol{v}}, \qquad \boldsymbol{\Sigma}_{\boldsymbol{v}} = \begin{pmatrix} \boldsymbol{\Sigma}_y + \boldsymbol{\Sigma}_\delta & 0 \\ 0 & 0 \end{pmatrix}. \tag{46}$$

The surrogate model covariance matrix $\boldsymbol{\Sigma}_\eta$ is given by applying the covariance function (44) onto each pair of $n+m$ input settings. The $n \times n$ observation covariance matrix is defined as $\boldsymbol{\Sigma}_y$ and (45) is applied to each variable input setting pair to obtain the $n \times n$ discrepancy covariance matrix $\boldsymbol{\Sigma}_\delta$. Following Bayesian inference, the posterior distribution of all the parameters conditional on the joint dataset can be obtained.

$$\begin{aligned}\pi\big(\boldsymbol{\theta}, \lambda_\eta, \lambda_\delta, \boldsymbol{\rho}_\eta, \boldsymbol{\rho}_\delta \big| D\big) &\propto L\big(D \big| \boldsymbol{\theta}, \lambda_\eta, \lambda_\delta, \boldsymbol{\rho}_\eta, \boldsymbol{\rho}_\delta, \boldsymbol{\Sigma}_y\big) \\ &\times \pi\big(\lambda_\eta\big) \times \pi\big(\boldsymbol{\rho}_\eta\big) \times \pi(\lambda_\delta) \times \pi(\boldsymbol{\rho}_\delta).\end{aligned} \tag{47}$$

Posterior realizations of the parameters can be drawn by MCMC methods Metropolis and Hastings sampling.

Predictions of the physical outcome at new inputs $(\boldsymbol{x}', \boldsymbol{t}')$ can be obtained conditional on the MCMC samples and data. The predictions, simulation output, and experimental data will have the joint distribution

$$\begin{pmatrix} D \\ \zeta^* \end{pmatrix} \sim N\left(\begin{pmatrix} 0 \\ 0 \end{pmatrix}, \begin{pmatrix} \boldsymbol{\Sigma}_D & \boldsymbol{\Sigma}_{D,\zeta^*} \\ \boldsymbol{\Sigma}_{\zeta^*,D} & \mathrm{diag}\left(\lambda_\eta^{-1}\right) \end{pmatrix}\right), \tag{48}$$

where the predictions of the physical system, ζ^* can be drawn through applying conditional normal rules [61]:

$$(\zeta^*|D) \sim N\left(\boldsymbol{\Sigma}_{\zeta^*,D}\boldsymbol{\Sigma}_D^{-1}D, \mathrm{diag}\left(\lambda_\eta^{-1}\right) - \boldsymbol{\Sigma}_{\zeta,D}\boldsymbol{\Sigma}_D^{-1}\boldsymbol{\Sigma}_{D,\zeta^*}\right). \tag{49}$$

Chapter 3: Experimental

3.1 Calibration Framework Overview

In this thesis, a framework is proposed to obtain fast and accurate predictions of a mesostructured material with a given material distribution x. We aim to minimize the residuals between prediction $\boldsymbol{y_p}(\boldsymbol{x})$and experimental result $\boldsymbol{y}(\boldsymbol{x})$, using calibrated material parameters $\boldsymbol{\theta}$ while accounting for uncertainties. By integrating physical experiments and simulations, the framework is able to calibrate unknown parameters $\boldsymbol{\theta}$, and represent the simulator as a surrogate model $\eta(\boldsymbol{x}, \boldsymbol{\theta})$, while accommodating for its inadequacies through the implementation of a discrepancy term $\delta(\boldsymbol{x})$.

The surrogate model $\eta(\boldsymbol{x}, \boldsymbol{\theta})$ is meant to be a statistical approximation of the simulations, which is based in GP models. Estimations of our calibration parameters with quantified uncertainty can be found through model updating, where these calibrated values will be used to make predictions. The model output can then be validated through a hold-out process to test the prediction accuracy. Given poor accuracy, further sampling of either experimental or simulation data can be conducted until satisfactory results are found.

The calibration framework is applied to a simple mechanical problem of a multi-material design. Mesostructured beams consisting of two materials with largely differing mechanical behavior are tested through three-point bending. We aim to solve the forward problem of predicting the maximum displacement of the material system. Additional to displacement data, we also obtain DIC images during testing to examine how the mesoscale design can influence the mechanical behavior. The simulations are found by applying continuum mechanics and constitutive modeling aided with FEA.

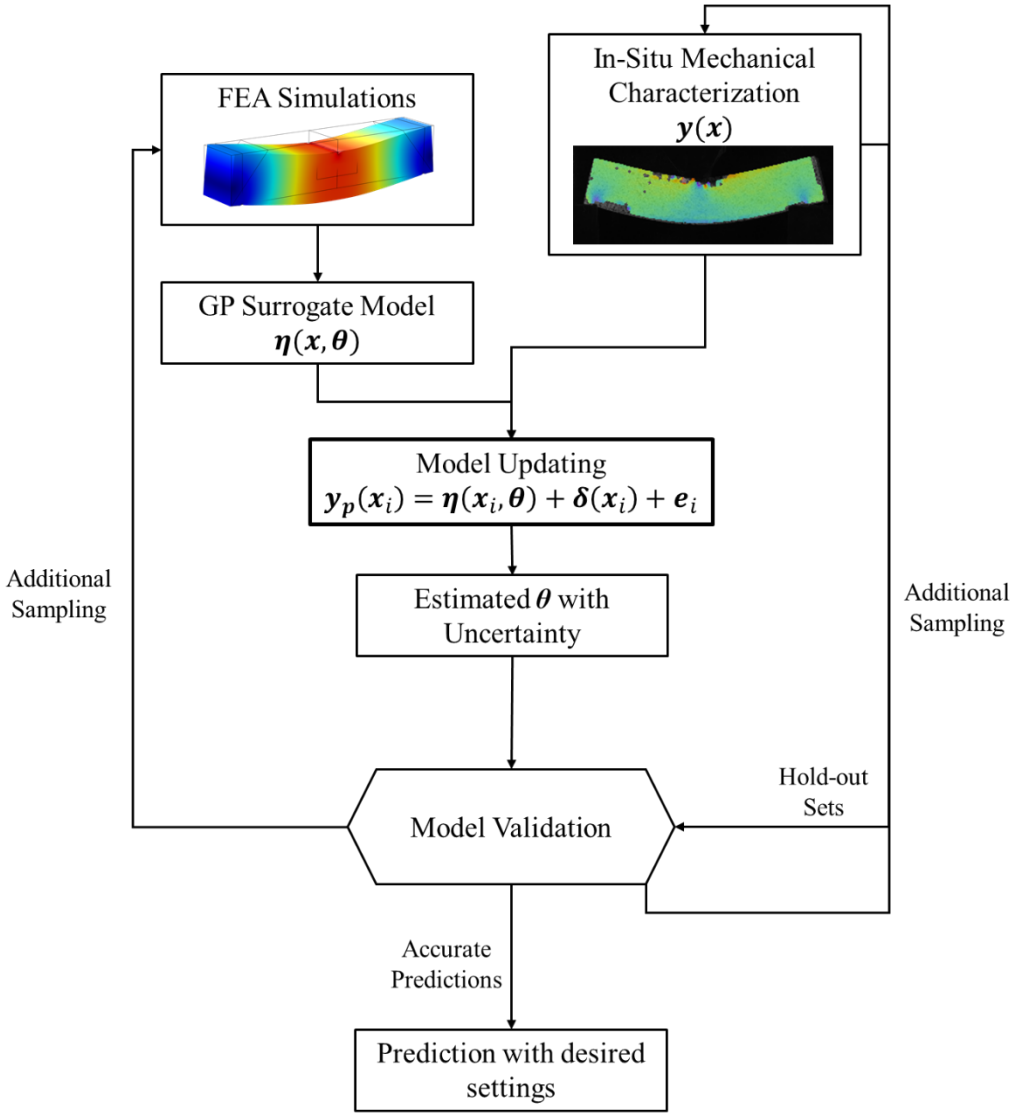

Figure 2. Bayesian calibration framework

3.2 Physical Experiments

Mesostructured beam samples were fabricated with five different material distributions as shown in Figure 2 with dimensions of $20 \times 20 \times 100$ mm. The samples were printed with a nozzle temperature of 225 ℃ and scanning speed of 12 mm/s through a dual extrusion enabled Lulzbot Taz 3D Printer. The constituent materials are the stiff Taulman Bridge Nylon, and TPU based NinjaTek Ninja-flex, which are both proprietary materials. The materials selection was based on their printability and large difference in stiffness meant to account for the limitations of the other material. The printed samples were then tested with three-point bending with a 5969 Instron at a

strain rate of 0.5 mm/min, with the bottom loading contacts placed 5 mm from each edge and the top contact placed in the center.

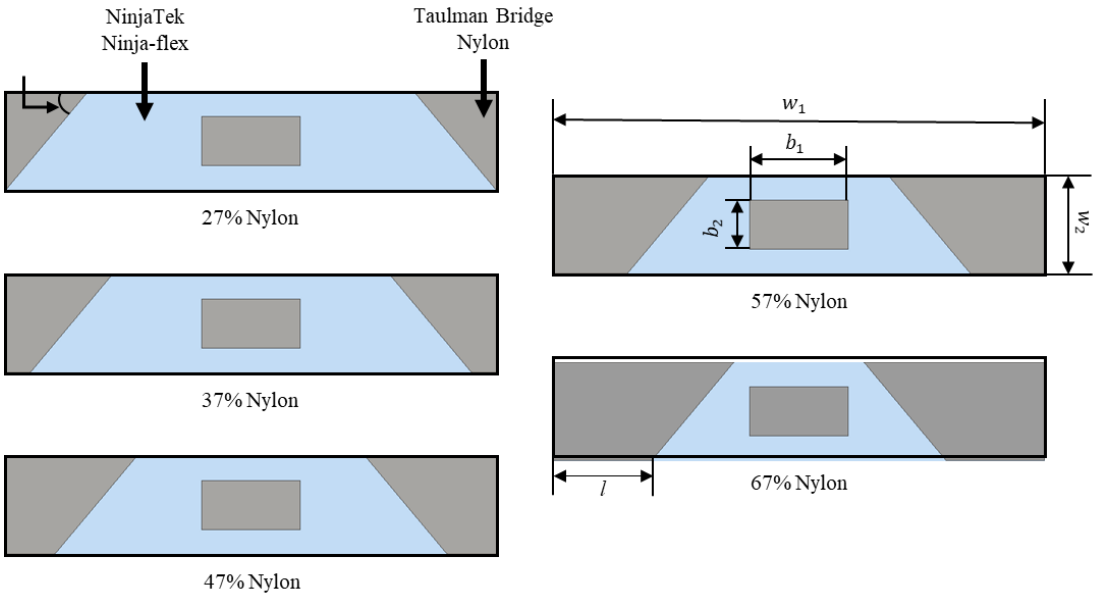

Figure 3. Five material distributions samples were fabricated at for mechanical testing

The templates shown in Figure 2 are simplified designs drawn from a previous multi-material design optimization study concerning beam bending [7]. Each sample is varied in material distribution that can be denoted by its nylon volume percentage, as shown in Figure 2, where the designs are dependent on the bottom length l. The interface angle α is set to $50°$, and the rectangular nylon section in the middle is defined by length $b_1 = 20\ mm$ and width $b_2 = 10\ mm$. The equation (50) is used to the define the material distributions, where w_1 and w_2 respectively correspond to the length and width of the full beam. The maximum displacement measurements of each sample are shown in Figure 3.

$$Nylon\ Volume\ Fraction = \frac{2(l \cdot w_2 + w_2^2 \cot(\alpha)) + b_1 \cdot b_2}{w_1 \cdot w_2}. \quad (50)$$

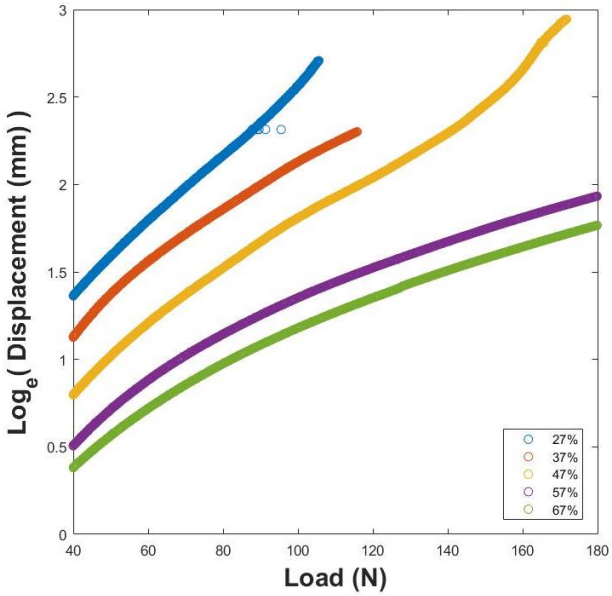

Figure 4. Experimental results of the maximum displacements for each mesostructured sample

In order to fully characterize the deformation behavior of our mesostructured samples and visualize the strain field redistribution, DIC images were taken during three-point bend testing using the zero normalized cross correlation criterion. Representative DIC images are shown in Figure 3 comparing the maximum tangential strain fields between a beam fully fabricated with the TPU material and a mesostructured beam with 47% nylon at the same time step. As expected of the pure TPU beam, the strain is distinctly concentrated around the center loading contact. For the mesostructured beam, it is clear that the strain is most notable at the boundary between the nylon and TPU material and not at the center contact point. It is important to note that the strain focused around the load is reduced because of the introduction of this mesoscale design. These DIC results verify that direct control of material distribution can allow for the redistribution of strain fields and thus impact local deformation behavior.

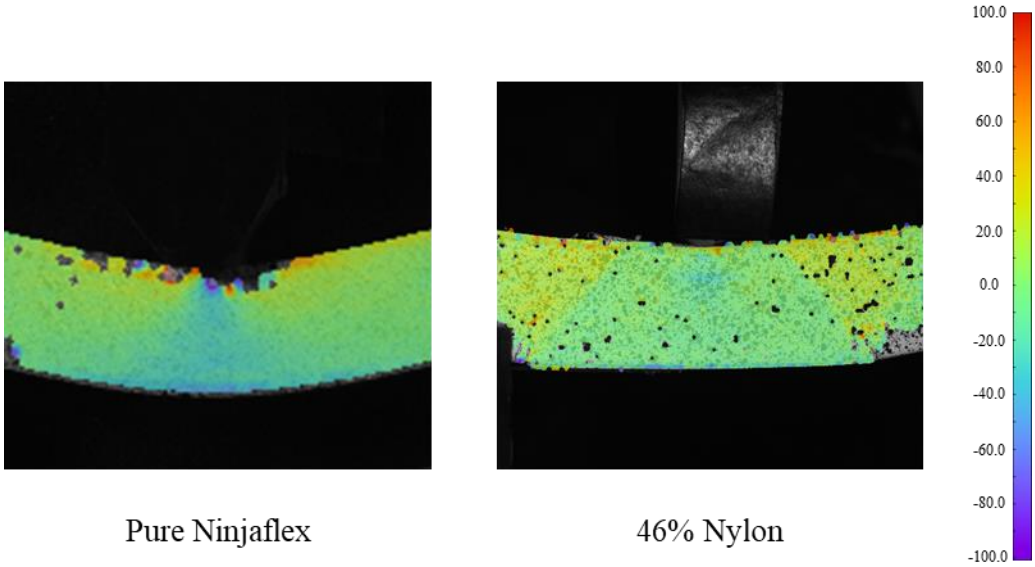

Figure 5. Maximum tangential strain distribution obtained by DIC of full TPU beam (left) and mesostructured 47% nylon beam (right) at the same time step

3.3 Model Development and Simulations

3.3.1 Constitutive Modeling

A 3D model containing the constitutive behavior of our mesoscale design to simulate its mechanical behavior can now be developed. The procedure involves defining the most appropriate constitutive models for the nylon and TPU materials, and the effective material parameters. Each individual material was characterized through the uniaxial tension test, under quasi-static loading, as shown in Figure 4. The nylon material at low strains showed an elastic-plastic behavior whereas the TPU material had a non-linear stress-strain relationship displaying hyperelasticity.

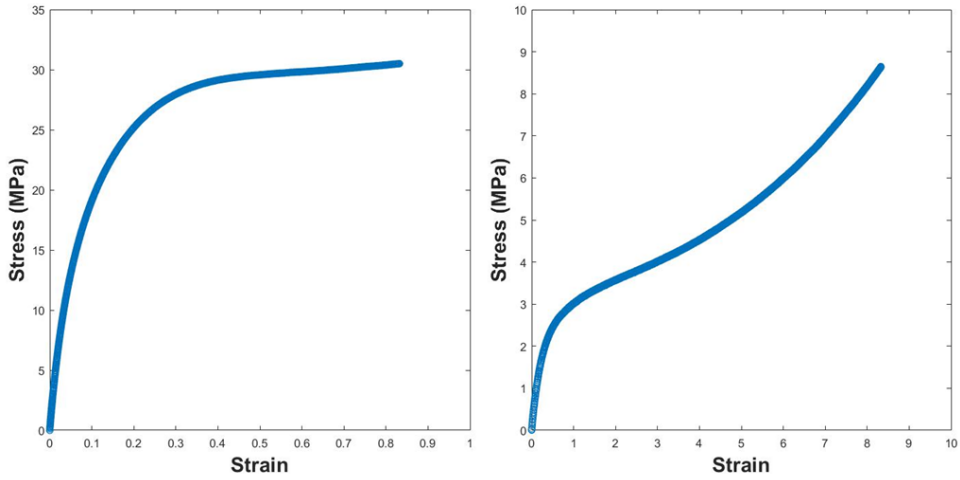

Figure 6. Stress-strain curve for nylon material (a) and stress-strain curve for TPU (b) obtained from uniaxial tension testing

The nylon showed a linear regime up to 6% axial strain and since we were trying to model for smaller deformations, the linear elastic model was selected. The linear regime gave measured values of Young's modulus of $E = 190$ MPa and Possion's ratio of $\nu = 0.46$. On the other hand, the hyperelastic TPU can be modeled using the Mooney-Rivlin model which has 5 parameters, $C_{10}, C_{01}, C_{11}, C_{20}$, and C_{02}. The model relates the first, I_1, and second, I_2, invariant of the unimodular component of the left Cauchy-Green deformation tensor, to the strain energy density W_s [73], [74].

$$W_s = C_{10}(I_1 - 3) + C_{01}(I_2 - 3) + C_{20}(I_1 - 3)^2 + C_{02}(I_2 - 3)^2 + C_{11}(I_1 - 3)(I_2 - 3). \quad (51)$$

Initial values for the five Mooney-Rivlin parameters are $C_{10} = -2.38, C_{01} = 5.37, C_{11} = -0.012, C_{20} = 0.004$ and $C_{02} = 0.69$ MPa and are found from fitting the model to the observed stress-strain curve.

Although single material testing can provide useful insight of the constitutive behavior and effective material parameters, it is likely insufficient for predicting the behavior of printed mesostructured materials. Manufacturing processes can have a large effect on many material parameter values as well as the microstructure. This is especially the case for multi-material additive manufacturing where the thermal and thermochemical processes can significantly differ between fabricating a single material tensile bar and a mesostructured system [1], [2], [4], [32],

[75]–[77]. Another important aspect is that since each material voxel is experiencing a multi-axial stress state, single material uniaxial tension testing is only valid for constitutive modeling if the materials show symmetric behavior in tension and compression, and if the material isotropic [49], [73]. For multi-material additive manufacturing this is not true, especially for polymers. Brittle polymers fail quicker in tension compared to compression, and hyperelastic solids show a strong pressure dependence and are almost incompressible [78]. Since the parameter values from material databases are not accurate for our problem, and specific material property information is not available for these proprietary materials, this necessitates parameter calibration.

3.3.2 Finite Element Analysis Simulations

As mentioned before, the constitutive models that were developed can be used to simulate the three-point bending behavior of our material through finite element analysis. The simulations were carried out through COMSOL Multiphysics solver via the Matlab LiveLink. Boundary conditions applied to the 3D model include defining two fixed 2D edges on the bottom surface of the mesoscale design. The load contact point is also applied as a 2D edge load with equal load distribution. For the sake of computational efficiency, four load settings, 45N, 80N, 120N, and 170N, were tested for all simulations to represent the mechanical behavior of the material. Representative results of the FEA simulation are shown in Figure 5, where output from a single design setting is shown at the four loadings.

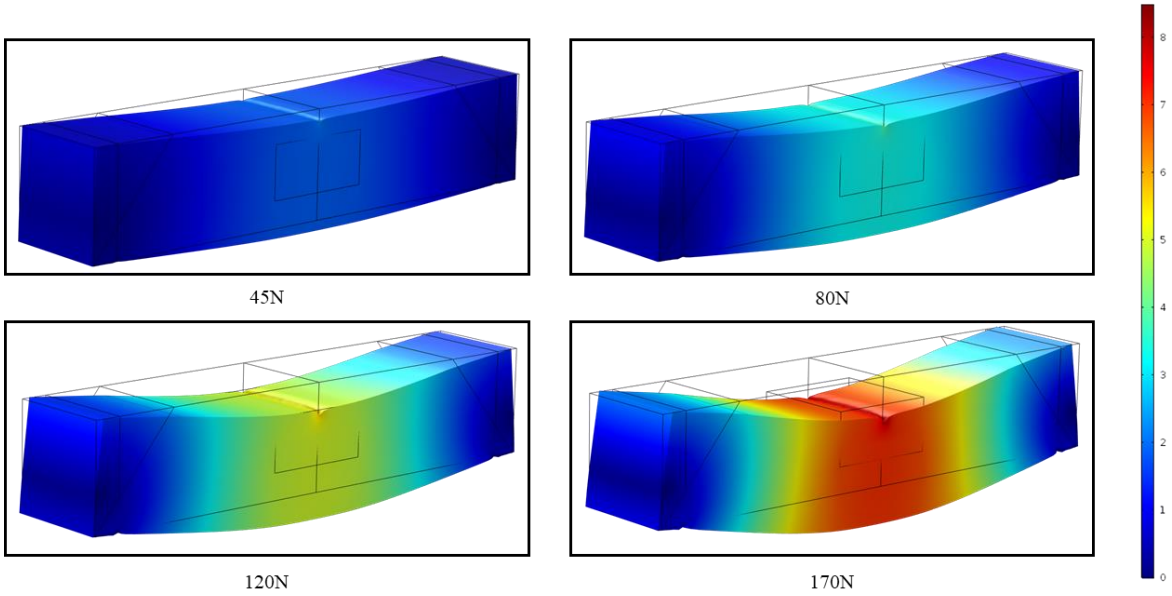

Figure 7. Representative simulation results of a 27% nylon design

Two sets of simulations were conducted, where the settings consist of the controllable variable inputs and the calibration inputs. For our problem, the variable input, x, is the nylon volume fraction, meant to denote the material distribution. The calibration inputs, $\boldsymbol{t}$, refer to context-specific inputs treated as unknowns, which would be our seven material parameters of interest, that will be calibrated. $\boldsymbol{\theta}$ represents the true calibrated versions of $\boldsymbol{t}$. The new notation for the total eight inputs is shown in Table 1.

Table 1. Notation for variable and calibration inputs

Original	Nylon Volume Fraction	E	ν	C_{10}	C_{01}	C_{11}	C_{20}	C_{02}
New	x	t_1, θ_1	t_2, θ_2	t_3, θ_3	t_4, θ_4	t_5, θ_5	t_6, θ_6	t_7, θ_7

Space filling Latin Hypercube (LH) designs are used to create the calibration inputs at which to run the simulations at. These designs aim to spread values at even points throughout the input space. The upper and lower bounds for each calibration input space are specified in Table 2. An important step before calibration is that all design input values are scaled to lie in $[0, 1]$.

Table 2. Upper and lower bounds of calibration inputs

Input	Upper Bound	Lower Bound
x	0.16	0.76
E [MPa]	1450	50
ν	0.499	0.001
C_{10} [MPa]	-1.18954	-3.56862
C_{01} [MPa]	8.05065	2.68355
C_{11} [MPa]	-0.0186768	-0.0560304
C_{20} [MPa]	0.008184935	0.00206164
C_{02} [MPa]	1.035489	0.345163

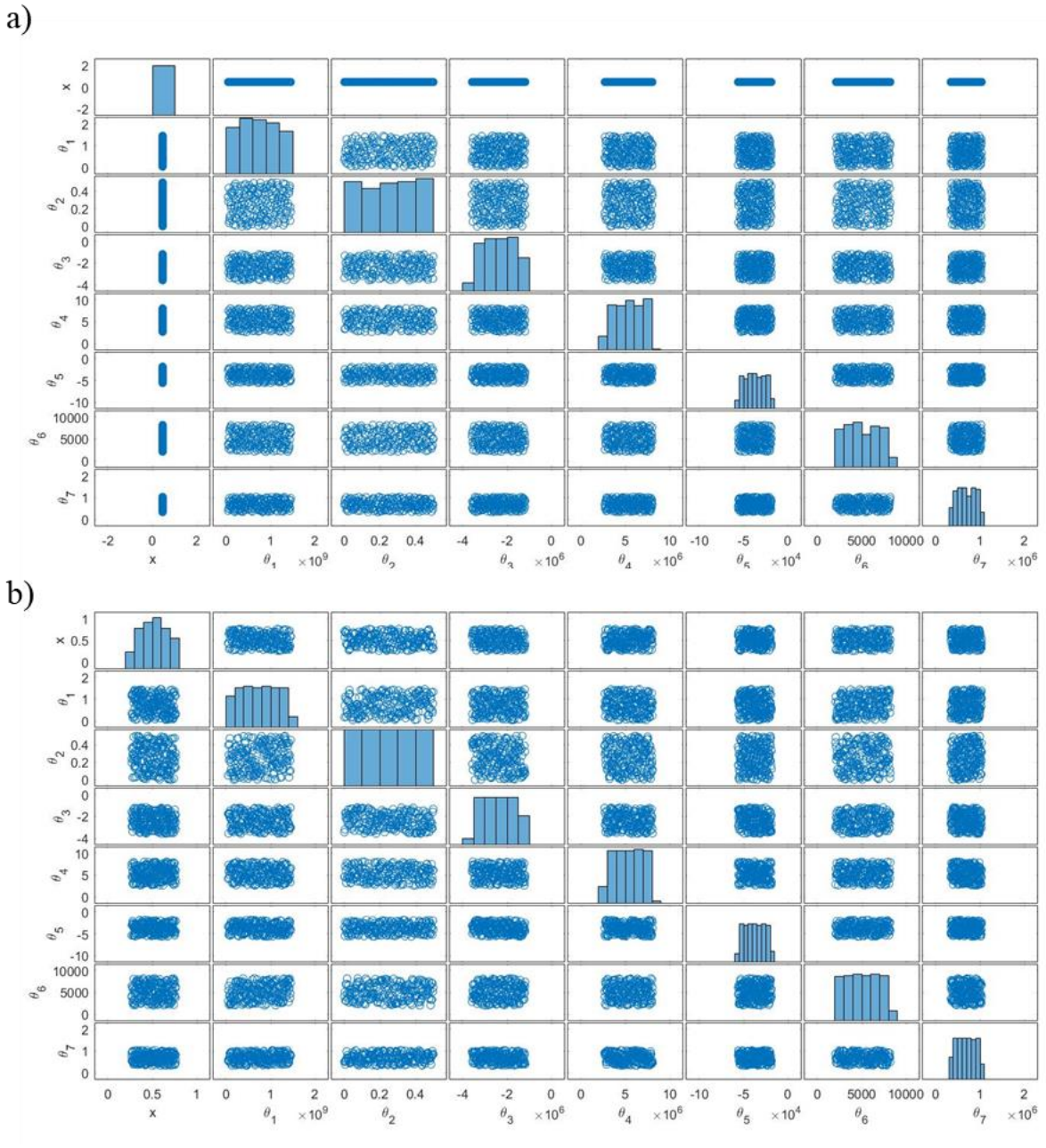

Figure 8. Scatter plot matrix of o_1=176 LH design for validation set (a) and o_2=200 Latin Hypercube design for training set (b)

The first set of $o_1 = 176$ simulations, which are shown in their native scale in Figure 6, were run with varied calibration parameters and a fixed $x = 0.46$ value. This set was not used for training but set aside for validating the surrogate model predictions. A second set of $o_2 = 200$ simulation

settings varying both calibration and variable inputs are run to be used to train the GP surrogate model.

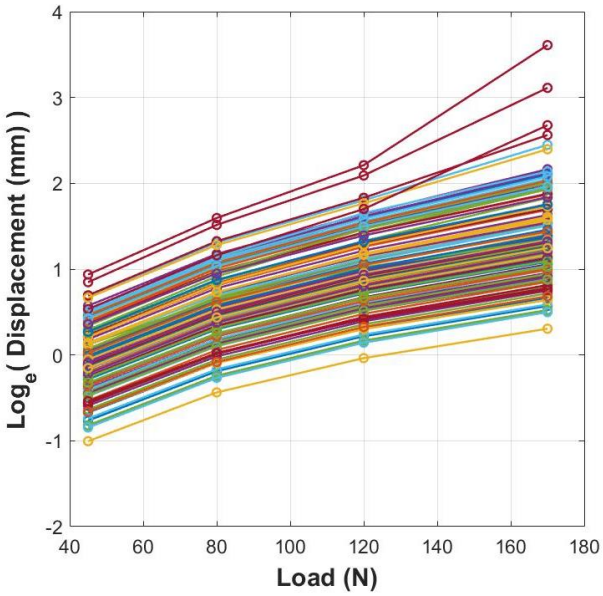

Figure 9. Simulation output of $m = 131$ runs

One issue that was encountered with the training simulation data is that for some input combinations, COMSOL did not converge. This led to about 69 simulation runs to be removed from the data set. The log displacement-load behavior of the remaining m =131 runs are plotted in Figure 7. The 69 design inputs that were filtered out are shown in their transformed scale in Figure 8. After examining these settings, we found there was not a clear trend if settings with low nylon composition values resulted in simulation errors. However, there was a notable amount of runs with low θ_3 and θ_4 values, where respectively 48 and 58 runs had values lower than 0.5. Most of the output showed similar load-displacement behavior except for 6 distinct runs that showed notable increases in displacement at the largest load setting, 170N.

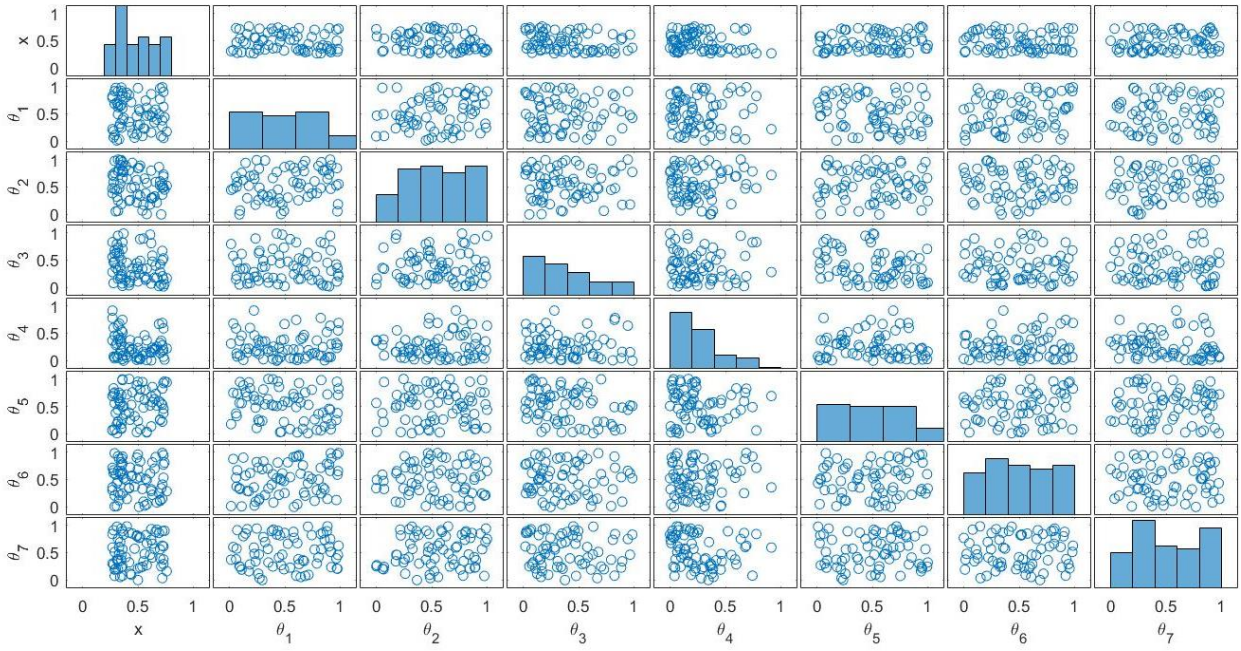

Figure 10. Scatter plot matrix of designs removed from training set

3.4 Bayesian Calibration

3.4.1 Surrogate Model Formulation

A Gaussian process surrogate model, also referred to as the emulator, can be constructed to predict the simulator output at untried inputs $(x, \boldsymbol{\theta})$. Since the analysis of the FEA simulations is difficult due to the high computational cost, the surrogate model is preferred. The surrogate model can be used to obtain fast predictions at any calibration and variable input value after being trained with the FEA simulation output. The simulation output is described with a basis representation.

$$\boldsymbol{\eta}(\boldsymbol{x}, \boldsymbol{t}) = \sum_{i=1}^{p_\eta} \boldsymbol{k}_i w_i(\boldsymbol{x}, \boldsymbol{t}) + \boldsymbol{\epsilon}. \tag{52}$$

Where k_i are the orthogonal basis vectors, the $w_i(x, t)$ are weights expressed as GP models placed over the input space, and ϵ is the n_η-dimensional error term. The basis vectors $\mathbf{K}_{\boldsymbol{\eta}} = \left[\boldsymbol{k}_1; \ldots; \boldsymbol{k}_{p_\eta}\right]$ are obtained by applying singular value decomposition (SVD) on the log transformed simulation output. The number of basis vectors to utilize is dependent on the application at hand, and in our

problem the $p_\eta = 2$ were selected. Generally, it is desirable to use basis vectors that capture at least 99% of the variance within the simulations. In this case, the first basis vector explains 99.86% and the second explains 0.13% satisfying this requirement. Plots of the first two principal components are shown in Figure 9.

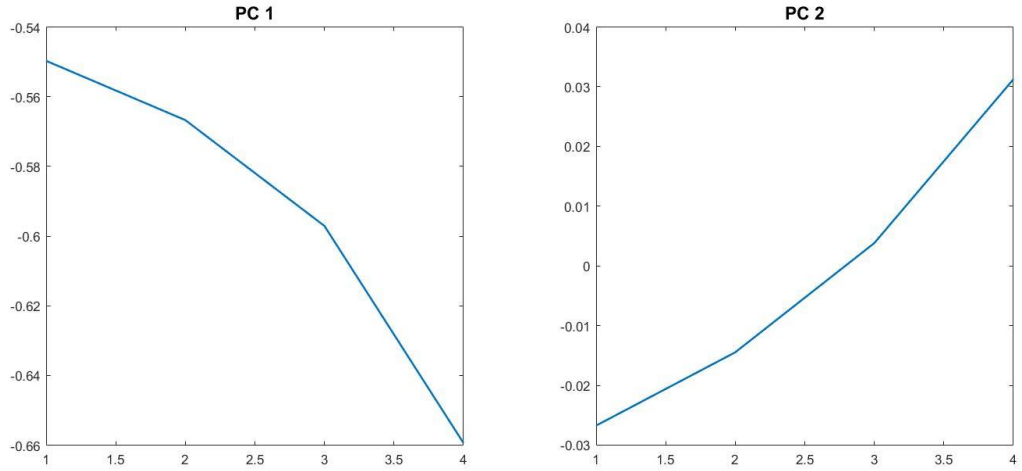

Figure 11. $p_\eta = 2$ principal components used for formulating surrogate model

As previously mentioned, the simulator output is modeled using basis representation. The corresponding PC coefficients $w_i(\boldsymbol{x}, \boldsymbol{t}), i = 1, \dots, p_\eta$, are then modeled as mean 0 GPs.

$$w_i(\boldsymbol{x}, \boldsymbol{t}) \sim \mathrm{GP}\left(0, \lambda_{wi}^{-1} R\left((\boldsymbol{x}, \boldsymbol{t}), \boldsymbol{x}', \boldsymbol{t}'\right); \boldsymbol{\rho}_{wi}\right). \tag{53}$$

PC coefficients are defined using the covariance function (43) with the marginal precision λ_{wi} and correlation distance ρ_{wi} defined for each input type. We can restrict this expression of $w(\cdot,\cdot)$ to the design inputs used for the simulations shown in Section 3.3.2. to an m-vector $\boldsymbol{w}_i$, as well as apply the covariance form (44) to each input settings pair to create an $m \times m$ correlation matrix. From here a prior distribution of the mp_η-vector $\boldsymbol{w} = \left(\boldsymbol{w}_1^T, \dots, \boldsymbol{w}_{p_\eta}^T\right)^T$ can be expressed with p_η precision parameters $\boldsymbol{\lambda}_w$ and $p_\eta(p_x + p_t)$ spatial dependence parameters $\boldsymbol{\rho}_w$:

$$\boldsymbol{w} \sim N\left(0_{mp_\eta}, \mathrm{diag}\left(\lambda_{wi}^{-1} \boldsymbol{R}\left((\boldsymbol{x}^*, \boldsymbol{t}^*); \boldsymbol{\rho}_{wi}\right); i = 1, \dots, p_\eta\right)\right) \tag{54}$$

Or

$$\boldsymbol{w} \sim N\left(0_{mp_\eta}, \boldsymbol{\Sigma}_w\right).$$

Independent gamma priors $\Gamma(a_w, b_w)$ for parameters $\boldsymbol{\lambda}_w$ and independent beta priors $\text{Beta}(a_{\rho_w}, b_{\rho_w})$ for parameters $\boldsymbol{\rho}_w$.

$$\pi(\lambda_{wi}) \propto \lambda_{wi}^{a_w-1} e^{-b_w \lambda_{wi}}, i = 1, \dots, p_\eta; \tag{55}$$

$$\pi(\rho_{wik}) \propto \rho_{wik}^{a_{\rho w}-1}(1-\rho_{wik})^{b_{\rho_w}-1}, i = 1, \dots, p_\eta, k = 1, \dots, p_x + p_t. \tag{56}$$

The gamma prior parameters were initialized at $a_w = 1$ and $b_w = 1.0 \times 10^{-5}$, and the beta priors for each input type was specified at $a_{\rho_w} = 1$ and $b_{\rho_w} = 0.1$. The initialization of these hyperparameters depend on the expected activity of the given inputs. With our specification, $\boldsymbol{\lambda}_w$ will have a fairly uninformative prior since it's expected that the data will be informative about the parameter. Another expectation from the simulator response is that it will follow "effect sparsity." So, our initialization of the beta priors places a high prior mass towards $\boldsymbol{\rho}_w = 1$.

Now the sampling distribution for the simulator output can be formulated combining expressions of the PC coefficients and the simulation precision. The mn_η-vector $\boldsymbol{\eta}$ can be described as

$$\boldsymbol{\eta} \sim N\left(0_{mn_\eta}, \boldsymbol{K}\boldsymbol{\Sigma}_w\boldsymbol{K}^T + \lambda_\eta^{-1}\boldsymbol{I}_{mn_\eta}\right). \tag{57}$$

Where $\boldsymbol{K}$ is the $mn_\eta \times mn_\eta$ matrix $\boldsymbol{K} = [\boldsymbol{I}_m \otimes \boldsymbol{k}_1; \dots; \boldsymbol{I}_m \otimes \boldsymbol{k}_{p_\eta}]$.

Given the surrogate model formulation, it is possible to make posterior predictions of the simulations at new input settings $(\mathbf{x}^*, \boldsymbol{t}^*)$. A predictive joint distribution of the data in basis space $\widehat{\boldsymbol{w}} = (\boldsymbol{K}^T\boldsymbol{K})^{-1}\boldsymbol{K}^T\boldsymbol{\eta}$ and predictions $\boldsymbol{w}(\boldsymbol{x}^*, \boldsymbol{t}^*)$ conditional on the parameters $(\lambda_\eta, \boldsymbol{\lambda}_w, \boldsymbol{\rho}_w)$ can be constructed, where predictions can be drawn using conditional normal rules.

$$\begin{pmatrix} \widehat{\boldsymbol{w}} \\ \boldsymbol{w}(\boldsymbol{x}^*, \boldsymbol{t}^*) \end{pmatrix} \sim N\left(\begin{pmatrix} 0 \\ 0 \end{pmatrix}, \begin{pmatrix} \boldsymbol{\Sigma}_{\widehat{w}} & \boldsymbol{\Sigma}_{\widehat{w},w^*} \\ \boldsymbol{\Sigma}_{w,\widehat{w}}^* & \text{diag}(\lambda_{wi}^{-1}; i = 1, \dots, p_\eta) \end{pmatrix}\right). \tag{58}$$

3.4.2 Discrepancy Model Formulation

As previously discussed, the physical outcome can be statistically modeled, combining simulation and experimental output to calibrate the calibration inputs while accounting for the discrepancy

from the simulations through the discrepancy term $\boldsymbol{\delta}(\boldsymbol{x})$. In this section, the formulation of this expression will be detailed.

Just like the surrogate model, basis representation is also used for formulating the discrepancy term, representing it as a linear combination of basis functions. However, in $\boldsymbol{\delta}(\boldsymbol{x})$ the basis vectors are usually nonorthogonal and the number of them depend on the application. Additionally, basis coefficients only depend on the variable input $\boldsymbol{x}$.

$$\boldsymbol{\delta}(\boldsymbol{x}) = \sum_{k=1}^{p_\delta} \boldsymbol{d}_k(\tau, \phi) v_k(\boldsymbol{x}) = \sum_{k=1}^{p_\delta} \boldsymbol{d}_k v_k(\boldsymbol{x}). \tag{59}$$

For our discrepancy model, $p_\delta = 6$ basis vectors were specified as a function over a grid of loads $0 \leq \mathrm{P} \leq 200$ with widths of 40. These specifications have shown smoothness along load space. As with the surrogate model, independent GP priors are placed on each coefficient $v_k(\boldsymbol{x})$. The basis vectors are specified as normal densities centered at each load from the grid with standard deviations of 40. These basis vectors are constructed for each experimental data set and normalized.

$$v_i(\boldsymbol{x}) \sim GP\left(0_i, \lambda_{vi}^{-1} \boldsymbol{I}_i \otimes R\big((\boldsymbol{x}, \boldsymbol{x}'); \boldsymbol{\rho}_{vi}\big)\right), i = 1, \dots, p_\delta. \tag{60}$$

The coefficients for each basis vector are specified as independent 0 mean GP priors as is shown in (59). The marginal precision λ_{vi}, spatial dependence parameter $\boldsymbol{\rho}_{vi}$ for each $\boldsymbol{x}$, and the stationary correlation function $R((\boldsymbol{x}, \boldsymbol{x}'); \boldsymbol{\rho}_{vi})$ are specified for the GP formulation of each coefficient. This GP form will match the expectations of a smooth variation of discrepancy along with the inputs.

$$\pi(\lambda_{vi}) \propto \lambda_{vi}^{a_v - 1} e^{-b_v \lambda_{vi}}; \tag{61}$$

$$\pi(\rho_{vi}) \propto \rho_{vi}^{a_{\rho_v} - 1} (1 - \rho_{vi})^{b_{\rho_v} - 1}, i = 1, \dots, p. \tag{62}$$

The hyperparameters for the discrepancy term is also defined by their corresponding gamma and beta priors. For the marginal precision, we specify $a_v = 1$ and b_v =0.001, and $a_{\rho v} = 1$ and $b_{\rho v} = 0.1$ for the spatial dependence parameters. Initialization for beta prior reflects the same expectation

of effect sparsity as with the surrogate model formulation. The marginal precision prior is meant to allow for smaller values leading to a larger role of the discrepancy.

3.4.3 Complete Model Formulation

The experimental observation data can now be modeled as the sum of the expressions of the surrogate and discrepancy model, with an observation error term described by $N(0_{n_{y_i}}, \left(\lambda_y \boldsymbol{W}_i\right)^{-\mathbf{1}})$**.** The experimental data set consists of $n = 5$ experiments as shown in Figure 3. Each dataset can be expressed as $\boldsymbol{y}(\boldsymbol{x}_i), i = 1, \dots, n$ with the inputs indexed by load settings.

$$\boldsymbol{y}(\boldsymbol{x}_i) = \boldsymbol{\eta}(\boldsymbol{x}_i, \boldsymbol{\theta}) + \boldsymbol{\delta}(\boldsymbol{x}_i) + \boldsymbol{e}_i. \tag{63}$$

With basis representation, the physical process can be shown as

$$\boldsymbol{y}(\boldsymbol{x}_i) = \boldsymbol{K}_i \boldsymbol{w}(\boldsymbol{x}_i, \boldsymbol{\theta}) + \boldsymbol{D}_i \boldsymbol{v}(\boldsymbol{x}_i) + \boldsymbol{e}_i. \tag{64}$$

The basis vectors $\boldsymbol{K}_i$'s can be obtained through interpolating from $\boldsymbol{K}_\eta$ because the support within the observations and simulations vary. The discrepancy basis vectors are found using the form (58) as previously mentioned. The sampling model of the full observation data can be formulated as n_y-variate normal where n_y refers to the total amount of data sets with the coefficients, $\boldsymbol{v} = \text{vec}([\boldsymbol{v}(\boldsymbol{x}_1); \dots; \boldsymbol{v}(\boldsymbol{x_n})]^T)$ and $\boldsymbol{u}(\boldsymbol{\theta}) = \text{vec}([\boldsymbol{w}(\boldsymbol{x}_1); \dots; \boldsymbol{w}(\boldsymbol{x}_n, \boldsymbol{\theta})]^T$.

$$\boldsymbol{y} \sim N\left(0_{n_y}, \boldsymbol{B}\ \text{diag}(\boldsymbol{\Sigma}_v, \boldsymbol{\Sigma}_u)\boldsymbol{B}^T + \left(\boldsymbol{\lambda}_y \boldsymbol{W}_y\right)^{-\mathbf{1}}\right). \tag{65}$$

The observation precision matrix is expressed as $\boldsymbol{W}_y = \text{diag}(\boldsymbol{W}_1, \dots, \boldsymbol{W}_n)$ for each experiment along with the precision λ_y, and the concatenation of the basis vectors are shown as $B = [\text{diag}(D_1, \dots, D_n); \text{diag}(\boldsymbol{K}_1, \dots, \boldsymbol{K}_n)]\ \text{diag}(\boldsymbol{P}_D^T, \boldsymbol{P}_K^T)$. The $\boldsymbol{P}_D^T$ and $\boldsymbol{P}_K^T$ terms are permutation matrices necessary for specifying $\boldsymbol{B}$. The observational error precision term λ_y is initialized with an informative gamma prior $\Gamma(a_y, b_y)$ with hyperparameter specifications of $a_y = 5\ and\ b_y = 5$. The discrepancy covariance matrix $\Sigma_v = \text{diag}(\lambda_{vi}^{-1}\ \boldsymbol{I}_i \otimes \boldsymbol{R}(\boldsymbol{x}; \boldsymbol{\rho_{vi}}); i = 1, \dots, p_\delta)$ defined by the $n \times n$ correlation matrix $\boldsymbol{R}(\boldsymbol{x}; \boldsymbol{\rho_{vi}})$ found from applying the covariance function (44) to each experimental input x . Similarly, the covariance matrix $\Sigma_u = \text{diag}(\lambda_{wi}^{-1}\ \boldsymbol{R}\big((\boldsymbol{x}, \boldsymbol{\theta}); \boldsymbol{\rho}_{wi}\big); i =$

$1, \ldots, p_\eta$) is specified using the covariance function (43) onto each experimental input pair to obtain the $n \times n$ correlation matrix $\boldsymbol{R}\big((\boldsymbol{x}, \boldsymbol{\theta}); \boldsymbol{\rho}_{wi}\big)$.

A prior distribution of the joint sampling model of the combined observed experimental and simulation data in basis space can be specified with covariance matrices $\boldsymbol{\Sigma}_v, \boldsymbol{\Sigma}_u, \boldsymbol{\Sigma}_w$ and $\boldsymbol{\Sigma}_{u,w}$.

$$z \sim N\left(0_{n(p_\delta + p_\eta) + mp_\eta}, \boldsymbol{\Sigma}_z = \begin{pmatrix} \boldsymbol{\Sigma}_v & \mathbf{0} & \mathbf{0} \\ \mathbf{0} & \boldsymbol{\Sigma}_u & \boldsymbol{\Sigma}_{u,w} \\ \mathbf{0} & \boldsymbol{\Sigma}_{u,w}^T & \boldsymbol{\Sigma}_w \end{pmatrix}\right). \tag{66}$$

The cross-covariance matrix $\boldsymbol{\Sigma}_{u,w} = \text{diag}(\lambda_{wi}^{-1}\boldsymbol{R}\big((\boldsymbol{x}, \boldsymbol{\theta}), (\boldsymbol{x}^*, \boldsymbol{t}^*); \boldsymbol{\rho}_{wi}\big); i = 1, \ldots, p_\eta)$ is defined by its $n \times m$ cross-correlation matrix $\boldsymbol{R}\big((\boldsymbol{x}, \boldsymbol{\theta}), (\boldsymbol{x}^*, \boldsymbol{t}^*); \boldsymbol{\rho}_{wi}\big)$ given by applying (43) to each experimental input pair $(x_1, \theta), \ldots, (x_n, \theta)$ crossed with each simulator input pair $(x_1^*, t_1^*), \ldots, (x_m^*, t_m^*)$.

Since the joint sampling distribution $L(\boldsymbol{y}, \boldsymbol{\eta}| \cdot)$ of all the observations is multivariate normal, which involves significant computational load, it is possible to reduce this by defining the sampling and prior distribution in the basis space. The sampling distribution of the basis transformed data $\hat{\boldsymbol{z}} = \text{vec}(\big[(\boldsymbol{B}^T\boldsymbol{W}_y\boldsymbol{B}\big)^{-1}\boldsymbol{B}^T\boldsymbol{W}_y\boldsymbol{y}; (\boldsymbol{K}^T\boldsymbol{K})^{-1}\boldsymbol{K}^T\boldsymbol{\eta}])$ can be given as

$$\hat{\boldsymbol{z}} \sim N\left(0, \boldsymbol{\Sigma}_{\hat{z}} = \boldsymbol{\Sigma}_z + \begin{pmatrix} \big(\lambda_y\boldsymbol{B}^T\boldsymbol{W}_y\boldsymbol{B}\big)^{-1} & 0 \\ 0 \quad 0 & \big(\lambda_\eta\boldsymbol{K}^T\boldsymbol{K}\big)^{-1} \end{pmatrix}\right). \tag{67}$$

Where the basis transformed prior distribution hyperparameters corresponding to $\boldsymbol{y}$ and $\boldsymbol{\eta}$ are specified as

$$a'_\eta = a_\eta + \frac{m\big(n_\eta - p_\eta\big)}{2}; \tag{68}$$

$$b'_\eta = b_\eta + \frac{1}{2}\boldsymbol{\eta}^T(\boldsymbol{I} - \boldsymbol{K}(\boldsymbol{K}^T\boldsymbol{K})^{-1}\boldsymbol{K}^T)\boldsymbol{\eta}; \tag{69}$$

$$a'_y = a_y + \frac{n_y - \text{rank}(\boldsymbol{B})}{2}; \tag{70}$$

$$b_y' = b_y + \frac{1}{2}\boldsymbol{y}^T\left(\boldsymbol{W}_y - \boldsymbol{W}_y\boldsymbol{B}\left(\boldsymbol{B}^T\boldsymbol{W}_y\boldsymbol{B}\right)^{-1}\boldsymbol{B}^T\boldsymbol{W}_y\right)\boldsymbol{y}. \tag{71}$$

Combining all basis transformed expressions can finally form the full posterior distribution of parameters.

$$\begin{aligned}\pi\left(\lambda_\eta, \boldsymbol{\lambda}_w, \boldsymbol{\rho}_w, \lambda_y, \boldsymbol{\lambda}_v, \boldsymbol{\rho}_v, \boldsymbol{\theta}\middle|\boldsymbol{y}, \boldsymbol{\eta}\right) \propto \\ |\boldsymbol{\Sigma}_{\hat{z}}|^{-\frac{1}{2}}\exp\left[-\frac{1}{2}\hat{\boldsymbol{z}}^T\boldsymbol{\Sigma}_{\hat{z}}^{-1}\hat{\boldsymbol{z}}\right] \times \lambda_\eta^{a_\eta'-1}e^{-b_\eta'\lambda_\eta} \times \prod_{i=1}^{p_\eta}\lambda_{wi}^{a_w-1}e^{-b_w\lambda_{wi}} \\ \times \prod_{i=1}^{p_\eta}\prod_{k=1}^{p_x+p_t}\rho_{wik}^{a_{\rho w}-1}(1-\rho_{wik})^{b_{\rho w}-1} \times \lambda_y^{a_y'-1}e^{-b_y'\lambda_y} \times \prod_{i=1}^{p_\delta}\lambda_{vi}^{a_v-1}e^{-b_v\lambda_{vi}} \\ \times \prod_{i=1}^{p_\delta}\prod_{k=1}^{p_x}\rho_{vik}^{a_{pv}-1}(1-\rho_{vik})^{b_{\rho v}-1} \times I[\boldsymbol{\theta} \in C].\end{aligned} \tag{72}$$

The prior for the calibration inputs $\boldsymbol{\theta}$ limits the parameter to region $C = [0,1]$. From here MCMC sampling can be used to obtain realizations of the parameters from this posterior distribution. In total, 20000 samples were drawn from the posterior probability distribution. The spatial dependence parameters $\boldsymbol{\rho}_w, \boldsymbol{\rho}_v$, and calibration inputs $\boldsymbol{\theta}$ can be found from Metropolis updating by using a uniform proposal distribution centered at the current parameter value with a width of 0.2. Hastings updating with uniform proposals centered at current parameter values and width 0.3 times the current parameter value can be used for sampling the precision parameters $\lambda_\eta, \boldsymbol{\lambda}_w, \boldsymbol{\lambda}_y,$ and $\boldsymbol{\lambda}_v$. These widths were chosen due to the nature of the standardized data.

3.4.1 Predictions

Using our realizations of parameters, it is possible to generate predictions of the log displacement of our material $\boldsymbol{\zeta}(\boldsymbol{x}^*) = \boldsymbol{\eta}(\boldsymbol{x}^*, \boldsymbol{\theta}) + \boldsymbol{\delta}(\boldsymbol{x}^*)$ given new input setting $\boldsymbol{x}^*$. This can be accomplished by sampling basis coefficients $\boldsymbol{w}(\boldsymbol{x}^*, \boldsymbol{\theta})$ and $\boldsymbol{v}(\boldsymbol{x}^*)$ conditional on the posterior realizations instead since $\boldsymbol{\eta}(\boldsymbol{x}^*, \boldsymbol{\theta}) = \boldsymbol{K}\boldsymbol{w}(\boldsymbol{x}^*, \boldsymbol{\theta})$ and $\boldsymbol{\delta}(\boldsymbol{x}^*) = \boldsymbol{D}\boldsymbol{v}(\boldsymbol{x}^*)$. It is also possible to sample the new basis coefficients conditional on the basis transformed data.

So, when testing the emulator at new input setting $(\boldsymbol{x}^*, \boldsymbol{t}^*)$, $\boldsymbol{w}(\boldsymbol{x}^*, \boldsymbol{\theta})$ can be sampled to make this prediction. A joint distribution of the basis coefficient prediction $\boldsymbol{w}(\boldsymbol{x}^*, \boldsymbol{\theta})$ and the basis

transformed simulation data $\widehat{\boldsymbol{w}} = (\boldsymbol{K}^T\boldsymbol{K})^{-1}\boldsymbol{K}^T\boldsymbol{\eta}$, conditional on the parameters $(\lambda_\eta, \boldsymbol{\lambda}_w, \boldsymbol{\rho}_w)$ can be obtained. Surrogate model predictions can be also made by applying conditional normal rules as shown in Section 2.11.

$$\begin{pmatrix} \widehat{\boldsymbol{w}} \\ \boldsymbol{w}(\boldsymbol{x}^*, \boldsymbol{\theta}^*) \end{pmatrix} \sim N\left(\begin{pmatrix} 0 \\ 0 \end{pmatrix}, \begin{pmatrix} \boldsymbol{\Sigma}_{\widehat{w}} & \boldsymbol{\Sigma}_{\widehat{w},w^*} \\ \boldsymbol{\Sigma}_{w^*,\widehat{w}} & \mathrm{diag}(\lambda_{wi}^{-1}; i = 1, \dots, p_\eta) \end{pmatrix} \right). \tag{73}$$

To make a system log displacement prediction, a joint distribution of the basis coefficient predictions and the data $\hat{\boldsymbol{z}}$ conditional on the sampled parameters $(\lambda_\eta, \boldsymbol{\lambda}_w, \boldsymbol{\lambda}_y, \boldsymbol{\lambda}_v, \boldsymbol{\rho}_w, \boldsymbol{\rho}_v, \boldsymbol{\theta})$ can be specified.

$$\begin{pmatrix} \hat{\boldsymbol{z}} \\ \boldsymbol{v}(\boldsymbol{x}^*) \\ \boldsymbol{w}(\boldsymbol{x}^*, \boldsymbol{\theta}) \end{pmatrix} \sim N\left(\begin{pmatrix} 0 \\ 0 \\ 0 \end{pmatrix}, \begin{pmatrix} \boldsymbol{\Sigma}_{\hat{z}} & \boldsymbol{\Sigma}_{\hat{z},v^*} & \boldsymbol{\Sigma}_{\hat{z},w^*} \\ \boldsymbol{\Sigma}_{v^*,\hat{z}} & \mathrm{diag}(\lambda_{vi}^{-1}; i = 1, \dots, p_\delta) & 0 \\ \boldsymbol{\Sigma}_{w^*,\hat{z}} & 0 & \mathrm{diag}(\lambda_{wi}^{-1}; i = 1, \dots, p_\eta) \end{pmatrix} \right). \tag{74}$$

Chapter 4: Results & Discussion

4.1 Training Plan 1

As discussed in the methodology, the model was trained with 131 simulation runs and 5 observation data sets. We will denote this as Training Plan 1. Since using the entirety of the MCMC realizations can be difficult, a subset of 3000 samples out of 20000 were used for analysis.

Before examining the performance of the surrogate model, we can first evaluate the GP fit of the simulator data by looking at the posterior realizations for ρ_{wik}. As previously mentioned in Section 3.4, these parameters are used to specify the covariance function of the surrogate model basis weight $w_i(\boldsymbol{x}, \boldsymbol{t})$. ρ is related to the spatial dependence parameter β through the relationship

$$\rho = \exp\left[-\frac{\beta}{4}\right]. \tag{75}$$

There are ρ variables subscribed to every variable input and calibration input for each principal component. For our problem, since we use the first two principal components, there are in total 16 ρ parameters realizations can be drawn. The two principal components used to formulate the GP surrogate model sufficiently accounts for over 99.9% of the variance with 99.86% in the first and 0.13% in the second. Since the clear majority of signal is present in the first principal component, the ρ values in the second principal component are of less interest. The ρ samples for each input from the first principal component were plotted as boxplots shown in Figure 10.

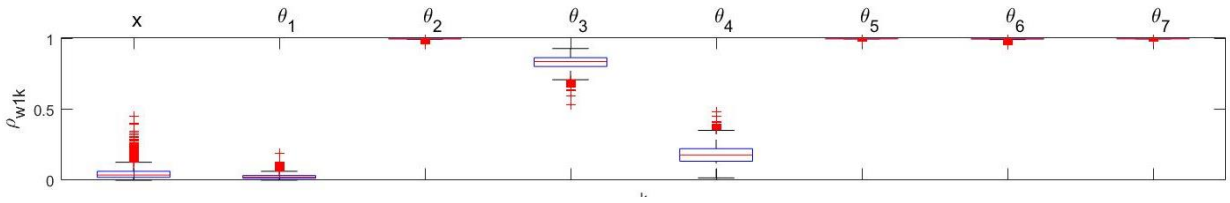

Figure 12. Boxplots of posterior realizations of ρ_{wik} parameter for each principal component

The ρ values can provide insight on the dependence between the simulator output and each input x and $\boldsymbol{\theta}$, which consequently affects the smoothness of the model output. If a specific input type shows $\rho = 1$, this refers to the simulation output remaining constant along the component. This indicates that there is no dependence between the output and the input, and thus knowing the value

of the input does not provide information to what the simulation result may be. This is the case for calibration inputs $\theta_2, \theta_5, \theta_6, \theta_7$ with ρ_{wik} values driven up to 1.

With decreasing ρ_{wik}, there is more dependence between the simulation output and input, where the output will vary smoothly along the input. However, when the parameter is driven down to 0, the smoothness is lost where the model starts fitting the data as noise because of the increased activity associated with the input. As we can observe from Figure 10, the model is most dependent on the calibration inputs θ_1, θ_3, and θ_4, and the variable input of x.

Since the prior for ρ was defined based on the belief that only a specific set of inputs would affect the model response, this result is expected. However, θ_1 showed a very low range of ρ indicating that the model response oscillates rapidly along this input, which can negatively influence the surrogate model's predictions. Further examination of the surrogate model's predictive capability has to be conducted before accepting output from the model.

The viability of the surrogate model was tested using a simple hold-out procedure. This involves training the model on the m simulation output that was specified in Section 3.3.2 and validating the predictions against a separate set of simulations. Compared to running simulations with FEA, the average computational load for making a single prediction with the surrogate model is much lower at 0.3286 *h*, whereas FEA simulations can take up to 40 minutes for each run.

The residuals for the predictions are shown in Figure 11. This shows that the surrogate model matches the simulation output closely with rare instances of larger residuals, where the errors are mostly from the model underestimating the simulator response. The difference between the emulator output and simulations can be calculated as the average root mean square error (RMSE). The average RMSE value was 0.1309, which is likely to be skewed higher due to the extreme outliers found in the residuals. When examining if there were any trends within the inputs associated with the prediction, a bias in error with θ_3 and θ_4 values lower than 0.5 was found. Out of the 17 predictions that showed residual values larger than 0.2 or lower than -0.2, there 13 instances where $\theta_3 < 0.5$ and 17 instances where $\theta_4 < 0.5$. This observation is consistent with the fact that since many simulations run at designs with low θ_3 and θ_4 values had to be removed from the training data, the surrogate model would have trouble predicting at these inputs. Additionally,

considering that these two inputs have the largest effect on the model response, it is unsurprising that they would also have an effect on the prediction residuals.

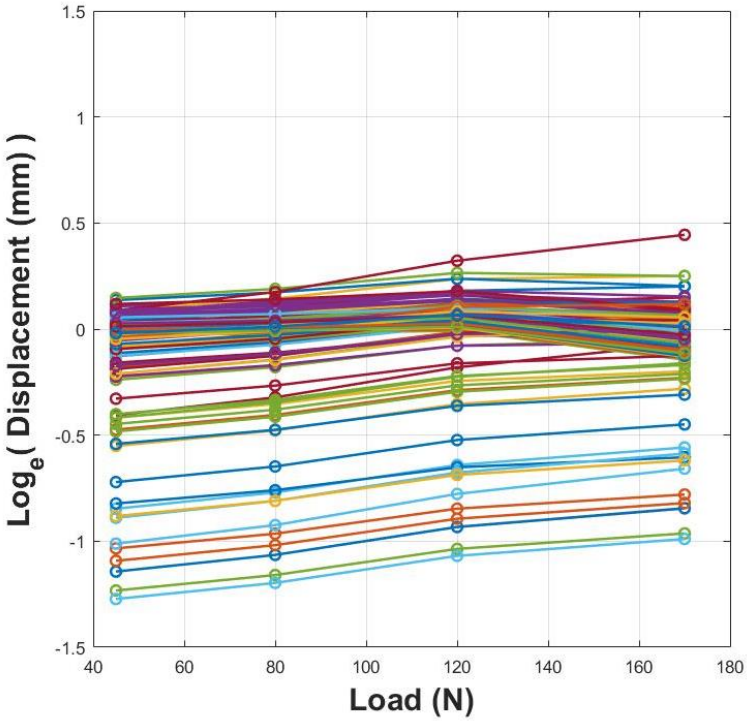

Figure 13. Surrogate model hold-out residuals

The sensitivity analysis results of the surrogate model are shown in Figure 12. The posterior mean estimates were calculated when varying a single input at values of [0.10 .30 .60 0.90] and holding the rest constant at 0.5. As previously defined, all inputs are normalized to range from 0 to 1. The darker lines in the plots refer to higher input values.

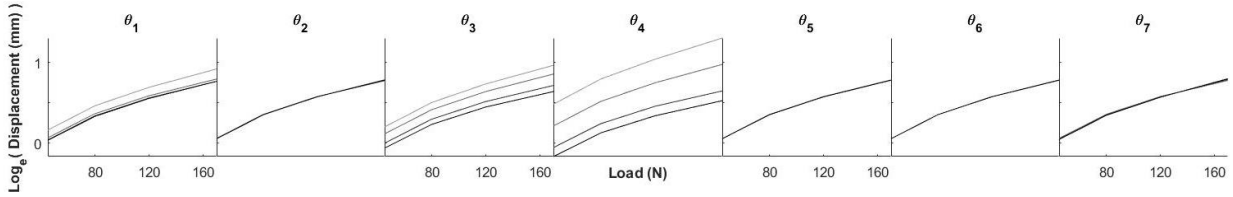

Figure 14. Sensitivity analysis of variable and calibration inputs

When observing the sensitivity plots, the calibration inputs $\theta_2, \theta_5, \theta_6, \theta_7$ show no effect on the output which agrees with what we observe in the boxplots of Figure 10. Input θ_1 shows minimal

effect on the surrogate model except at the lowest value of $\theta_1 = 0.1$. The nylon volume fraction variable x and calibration input θ_4 show the largest influence over the output followed by a lesser effect from θ_3. This sensitivity from the material distribution meets expectations of the multi-material design having a large effect on the mechanical behavior of the mesostructure.

The sensitivity analysis suggests that the marginal effect of θ_1 is minimal with the exception of when the input is set to 0.1, despite the activity associated with the input observed in Figure 10. The interactions between θ_1 and each input θ_3 and θ_4 were explored by observing the joint effect the variation in each input value has on the basis weight $w_1(x, \boldsymbol{t})$, which is shown as a mean surface in Figure 13. From these surface plots, noticeable interactions between the calibration inputs were not found, indicating that θ_1 was not modifying the effect of θ_3 or θ_4. However, these surfaces provide more insight on how rapidly the model response changes at the lower range of θ_1. Thus, the very low realization values of ρ for this input allows for this very flexible model response along θ_1.

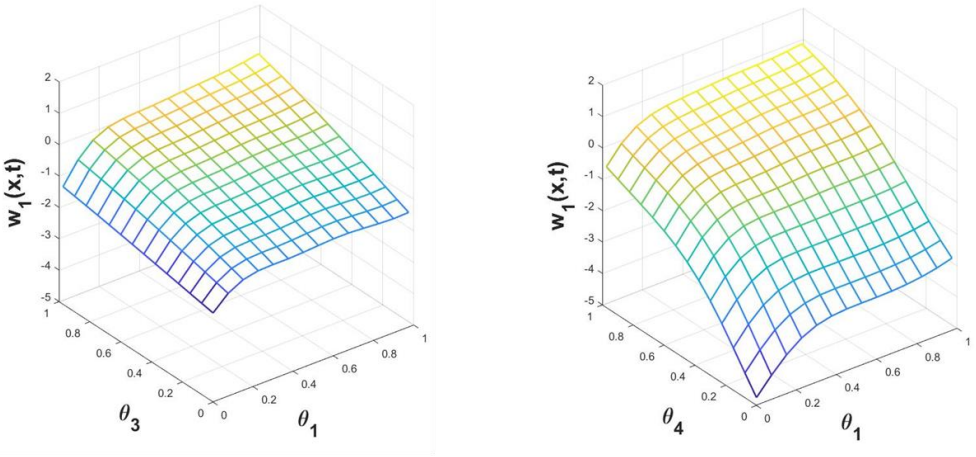

Figure 15. Posterior mean surface of basis weight $w_1(x, \boldsymbol{t})$ with varied θ_1 and θ_3 values (left) and varied θ_1 and θ_4 (right)

Conducting MCMC sampling of the posterior distribution provides insight on the calibrated material parameter values. The posterior MCMC realizations of the calibration inputs are shown as histograms in Figure 14. The parameters with most convergence are shown to be θ_1, θ_3, and θ_4 since they showed the highest effect on the surrogate model output. Parameter θ_1 shows a bimodal

distribution, but with a much larger bias towards the higher values, while θ_4 shows more weight in the lower range of the inputs and θ_3 converges more at a midpoint of the prior range.

This bimodal distribution for θ_1, which corresponds to the Young's modulus, can be due to the large difference in stiffness in the material at varied nylon volume fractions. The material stiffness can be dominated by either the TPU or nylon behavior leading to sampling very low or high Young's modulus values. As expected from the ρ parameter realizations and sensitivity analysis, θ_4 showed the largest convergence. The realizations of the rest of the inputs resembled a uniform distribution, which also matches expectations from previous analysis. The estimated means of each calibration input are listed in Table 3.

Table 3. Mean and variance of calibration parameters. For θ_1, the first and second entry correspond to the mean and variance of the smaller peak (low range) and larger peak (high range), respectively.

θ_1 [Pa]	θ_2	θ_3 [Pa]	θ_4 [Pa]	θ_5 [Pa]	θ_6 [Pa]	θ_7 [Pa]
2.80×10^8 $\pm9.29\times10^8$	0.25 ±0.13	-2.51×10^6 $\pm5.12\times10^5$	3.51×10^6 $\pm4.94\times10^5$	-3.73×10^4 $\pm1.09\times10^4$	5264.96 1782.43	7.06×10^5 1.99×10^5
1.24×10^9 $\pm1.29\times10^8$						

It can be noted that the estimated mean values of $\theta_2, \theta_5, \theta_6, \theta_7$ are of less importance because of the uniform distribution of their realizations and that any value from the given input range will give the same effect. Another point to note is that although the estimated mean of the Young's modulus is 1.1694 GPa, it is important not to completely disregard the realizations in the lower range.

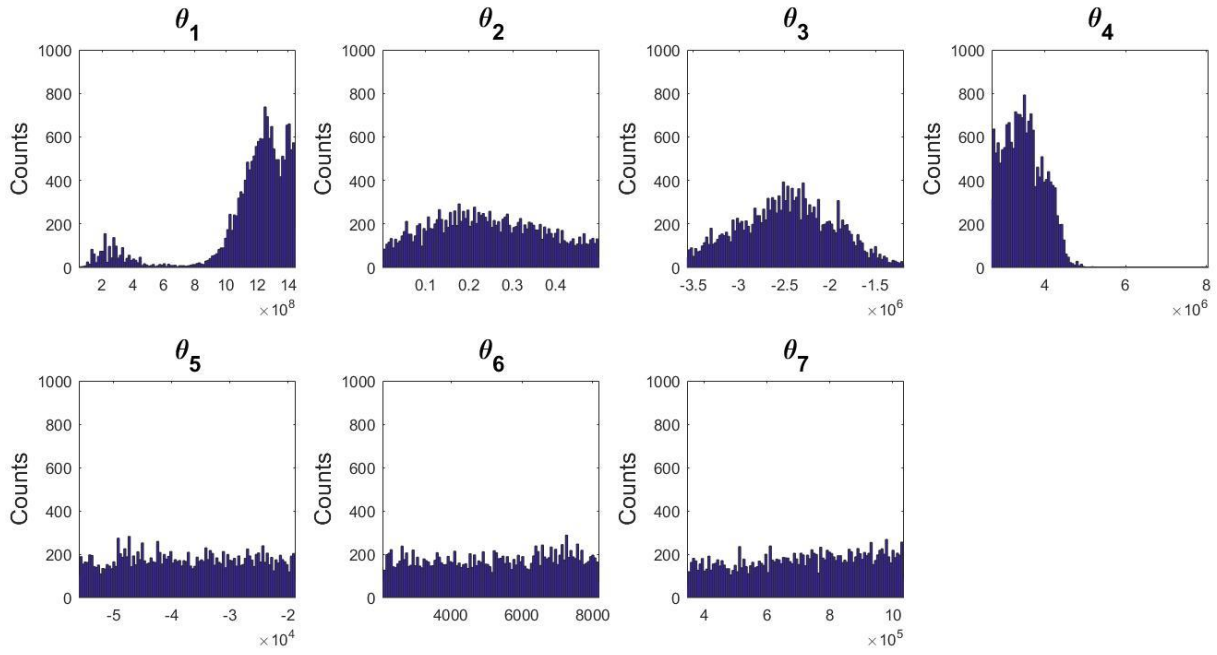

Figure 16. Posterior MCMC realizations of calibration inputs

Another aspect to explore is how the surrogate model response using calibrated model parameters differs from the simulation output that was used for training. Figure 15 shows representative examples when comparing the two responses. The simulations show much lower estimates of the displacement especially at the 67% nylon setting. This shows how predictions for the simulations can change given parameter calibration.

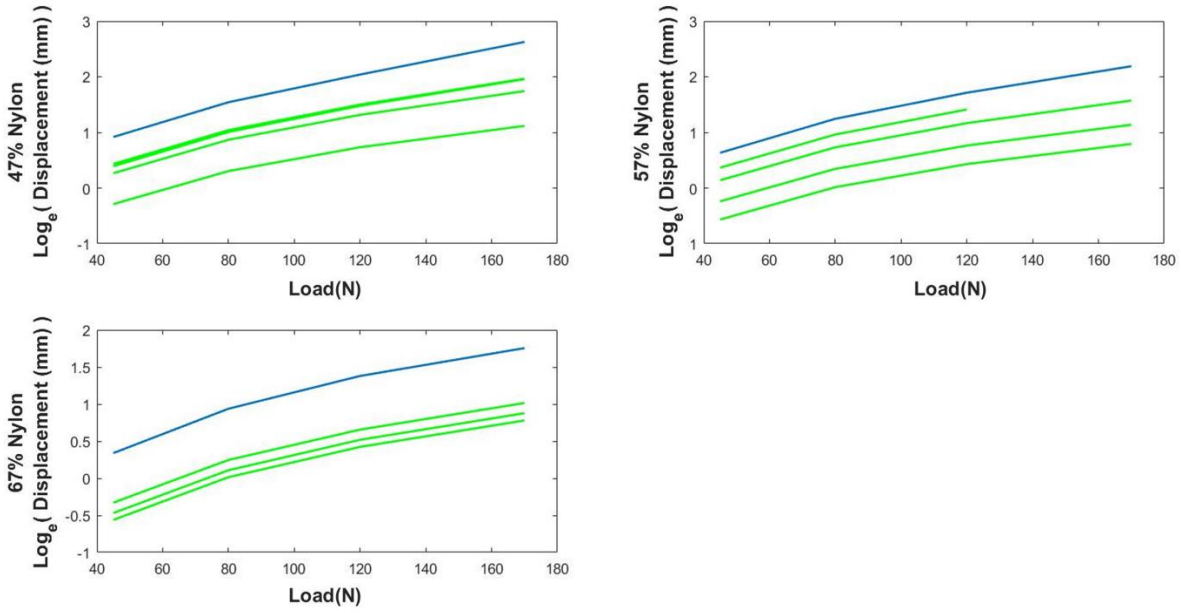

Figure 17. Comparison of surrogate model mean response (blue) and simulation output (green)

The posterior predictions through hold-out validations are shown in Figure 16. The results are broken down into the calibrated surrogate model response, discrepancy, and overall system prediction. The hold-out validation involves using experimental data of four of the samples and testing at the remaining material distribution. The bounds indicate the 5^{th} and 95^{th} percentiles to represent the uncertainty of the predictions. The predictions are plotted against the physical observations for each material distribution setting shown in blue. RMSE is also used to denote the difference between the estimated displacements and the measured values. The absolute residuals and RMSE values for the system predictions are shown in Table 4. The averaged RMSE for all the hold-out validations is 0.14 log displacement, which is less than 5% of the displacement range of 3 log displacement. We can compare these results against FEA simulations that were run using values from single material uniaxial tension testing, where the residuals and RMSE values are shown in Table 5. The average RMSE for these simulations were 0.76, showing a necessity of calibration to obtain accurate predictions.

Table 4. Absolute residuals and RMSE of system predictions using calibrated $\boldsymbol{\theta}$

	Absolute Residuals	**RMSE**

	45 N	80 N	120 N	170 N	
27%	0.03	0.08			0.06
37%	0.05	0.03			0.04
47%	0.15	0.17	0.07	0.46	0.25
57%	0.07	0.14	0.23	0.44	0.26
67%	0.22	0.14	0.08	0.03	0.13

During these hold-outs, the discrepancy model response is consistently minimal except for when validating for the 47% nylon sample. The discrepancy allows for an upward correction at lower loads and then a downward correction at larger loads. The downward effect from the discrepancy is likely influenced by the more linear response present at higher nylon volumes of 57% and 67%, since the sudden increase in displacement characteristic of elastic behavior is not known during this hold-out set.

Another notable aspect of the hold-outs is the uncertainties for each prediction. The predictions at 27%, 47%, and 67% show the largest uncertainties at each load, where for the 47% prediction, the discrepancy reduces the initial uncertainty coming from the surrogate model. The larger uncertainties of the 27% and 67% predictions are likely due to the absence of observation training data beyond the nylon composition the model is trying to predict at. The large variation in simulation output for nylon volume percentages in the range of 40%-50% can contribute to the large uncertainty of the surrogate model response. Where at the load setting 170N, the simulation output can be as low as 1.1174 and as high as 3.6102. Additionally, for predictions at 27%, 37%, and 47%, the uncertainty is noticeably larger at 170N. This uncertainty can likely be attributed to observation training data at lower nylon levels not having data points at higher loads.

Table 5. Absolute residuals and RMSE of system predictions using $\boldsymbol{\theta}$ from single material uniaxial testing

	Absolute Residuals				**RMSE**
	45 N	**80 N**	**120 N**	**170 N**	

27%	0.68	0.79			0.73
37%	0.96	0.72			0.85
47%	0.56	0.59	0.70	1.23	0.81
57%	0.38	0.33	0.30	0.31	0.33
67%	0.39	0.31	0.28	0.29	0.32

We were able to achieve this accuracy despite limitations in the training data. To reiterate, the strain limits that were set during experimentation of the 27% and 37% nylon samples meant that important aspects of the material's physical behavior would not be included for some of the hold-out sets. Another limitation comes from the number of both experimental and simulation training data sets that were available when trying to predict the material behavior which can fluctuate largely given different material distributions. Out of the desired 200 simulation output sets, we were only able to use 131 runs for training, and over the range of 27%-77% nylon composition, only 5 different samples were tested experimentally.

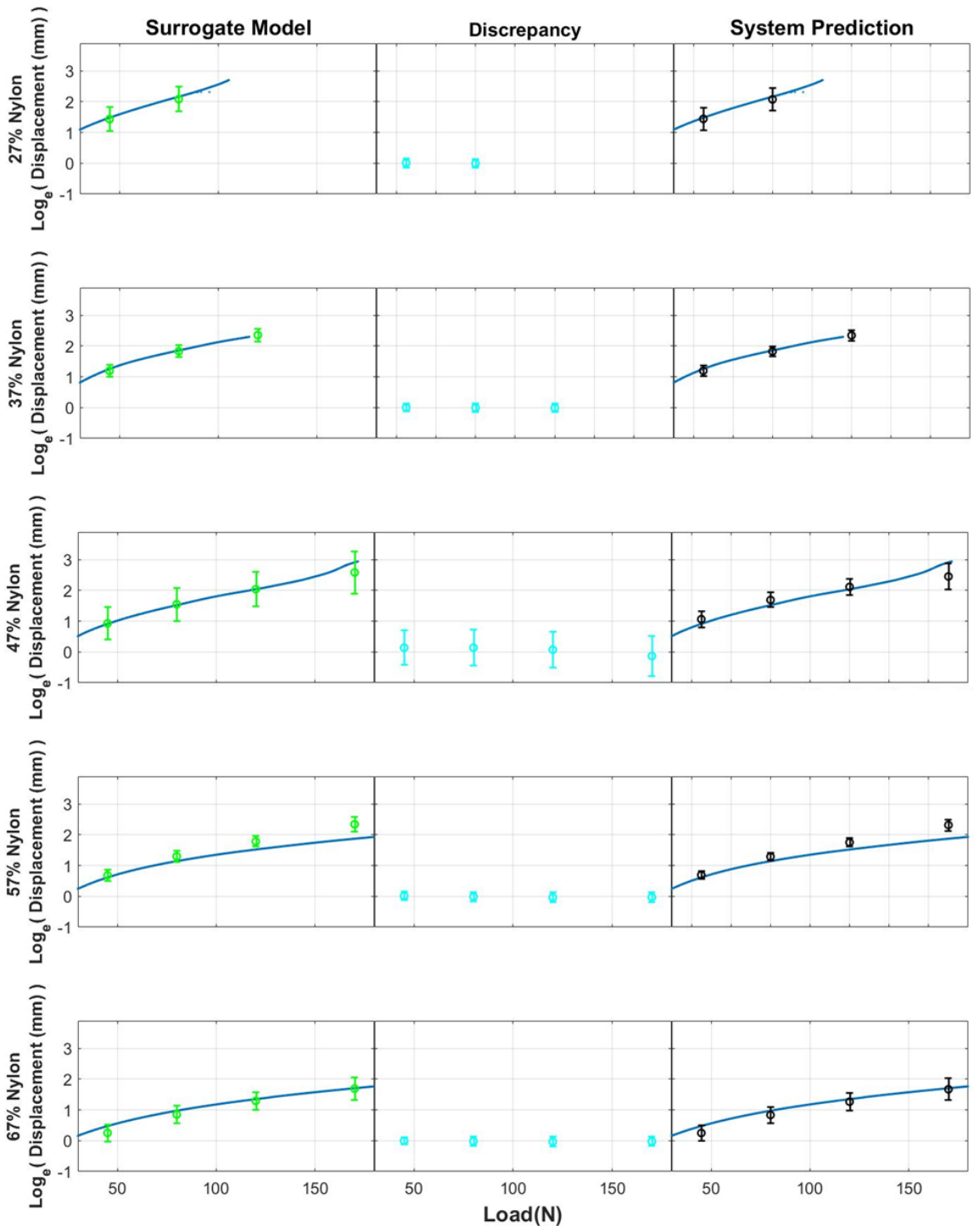

Figure 18. Posterior hold-out predictions at each experimental input. First column: 5th and 95th percentile bounds of surrogate model response (green) and experimental data (blue). Second column: 5th and 95th percentile bounds of posterior discrepancy. Third column: 5th and 95th percentile bounds of system prediction (black) and experimental data (blue).

From here, the effect that varied material distribution has on the posterior discrepancy model was explored further. Figure 17 illustrates mean response of the posterior discrepancy as a function of material distribution ranging from 27% to 77% nylon volume percentage. As expected, there is minimal effect coming from the discrepancy model with a small negative correction. This indicates that the simulations explain the physical behavior of the material sufficiently across the entire range of material distribution. The limited role of $\boldsymbol{\delta}(\boldsymbol{x})$ is generally more favorable when applying the predictive model in untested settings.

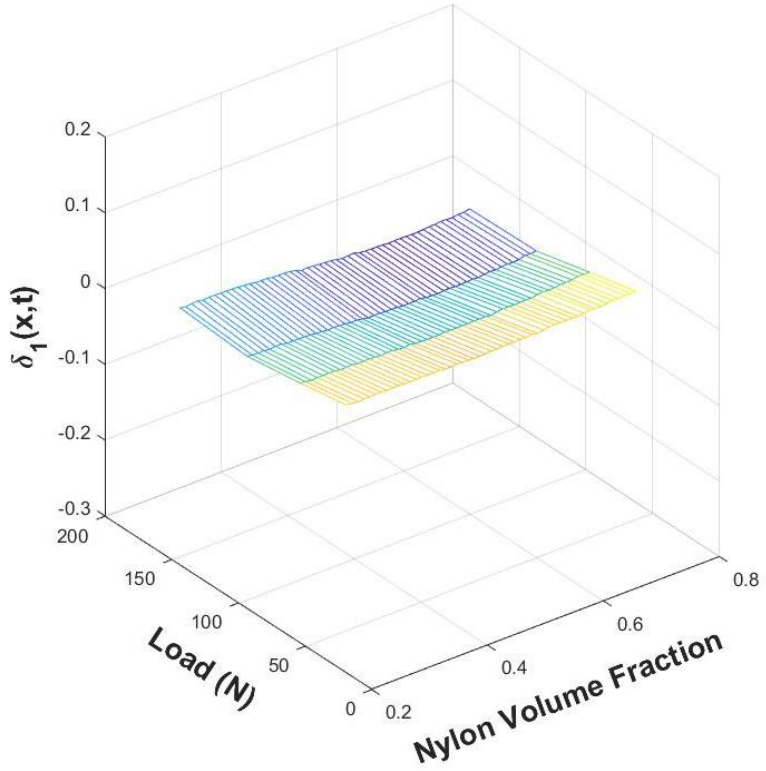

Figure 19. Posterior mean δ response as a function of material distribution

We can now demonstrate that with our calibrated statistical model, it is possible to predict the physical response of our mesoscale heterogeneous material system at any desired material distribution. In Figure 18, the responses from the system prediction is shown in 3D and 2D ranging in 27% to 77% in nylon volume percentage. From the two plots, it is clear that the predictive model is able to provide a realistic representation of the material's mechanical behavior. At higher nylon compositions, the load-displacement relationship is almost linear. With decreasing nylon, the

degree of displacement is noticeably increased at 170N, giving more of a non-linear load-displacement reponse characteristic of a material with dominant TPU behavior.

In summary, the calibration framework was successfully applied to our mesoscale design providing insight into the material parameters as well as a model allowing predictions at untested material distributions. The subset of calibration inputs θ_1, θ_3, and θ_4 were found to have the most influence on the model output. Hold-out validations at 5 different material distributions showed promising accuracy with an RMSE of 0.16 log displacement. The predictive model was able to effectively combine simulation and physical observation data to give an accurate representation of the material system.

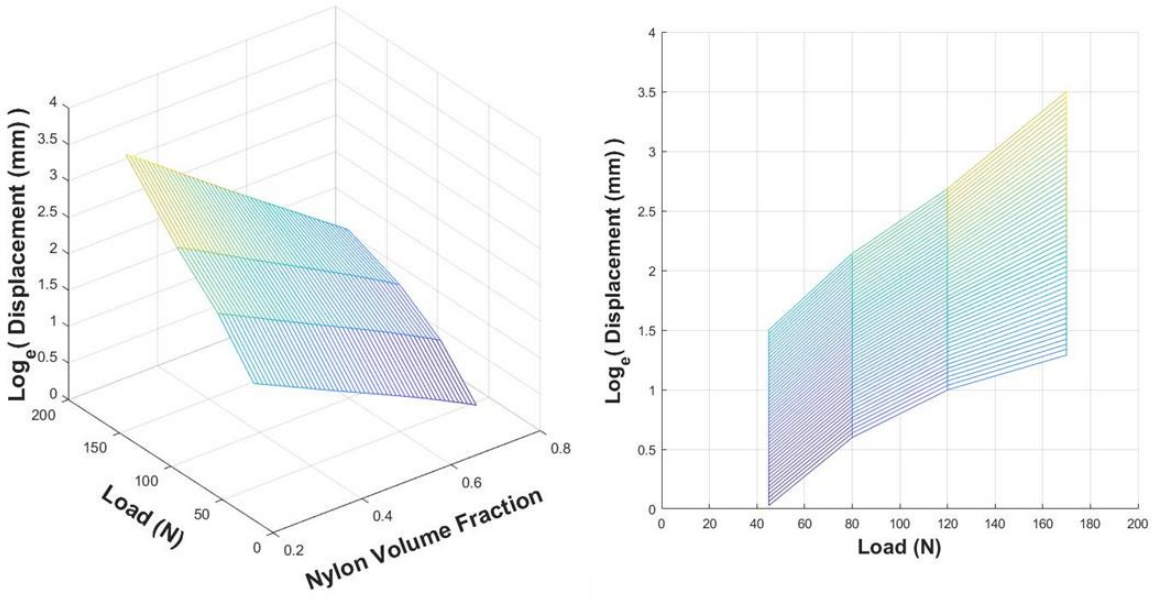

Figure 20. Posterior mean surface of the system prediction (left) and 2D load-displacement (right)

4.2 Training Plan 2

To explore how the model can account for the inadequacy in the simulator, a new training plan can be developed. From the 131 simulations that were used for training in Training Plan 1, 6 runs representative of the material at lower nylon composition where TPU dominant behavior is found, as marked in Figure 20 in red, were removed. So, 125 simulation runs, and the 5 observation data sets were used to train the model, where we denote this as Training Plan 2.

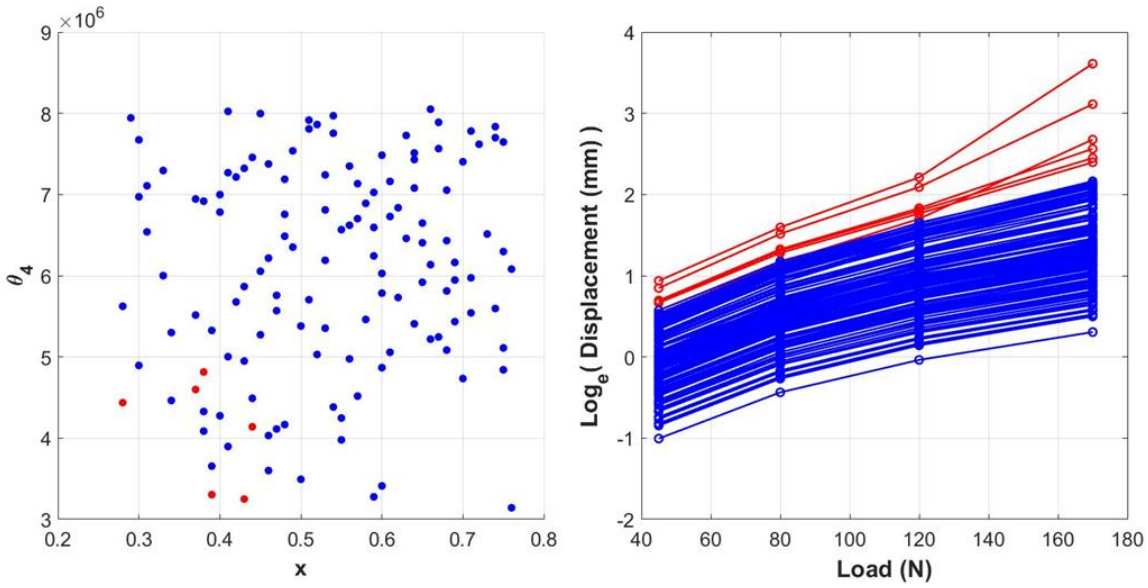

Figure 21. (a) x vs θ_4 scatter plot of the 131 simulation training data design, where the red points are the input settings excluded from Training Plan 2. (b) The 131 simulation training data where the runs marked in red are excluded for training plan 2

Training Plan 2 did not largely affect the posterior ρ realizations and sensitivity analysis. Meaning that θ_1, θ_3, and θ_4 are the only calibration inputs that have significant influence on the model output. One difference is with the posterior MCMC samples as shown in Figure 19. Under this training plan, the realizations of θ_3 converge at its lower range instead of the midpoint.

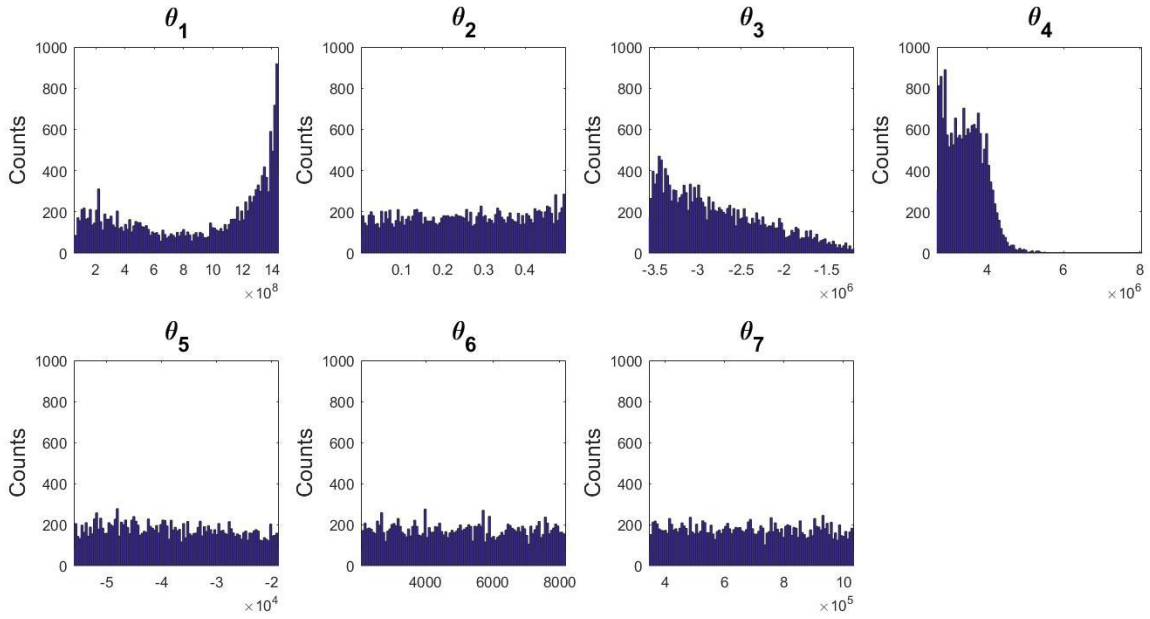

Figure 22. Posterior MCMC realizations of calibration inputs for Training Plan 2

To compare the surrogate model performance between the two training plans, the same hold-out validation with the simulation data is conducted as shown in Figure 20. The overall accuracy of the surrogate model is reduced as expected because of the further limited simulations used for

training, with an average RMSE value was 0.25. The errors showed similar trends with the inputs where there were larger residuals for settings with lower θ_3 and θ_4 values.

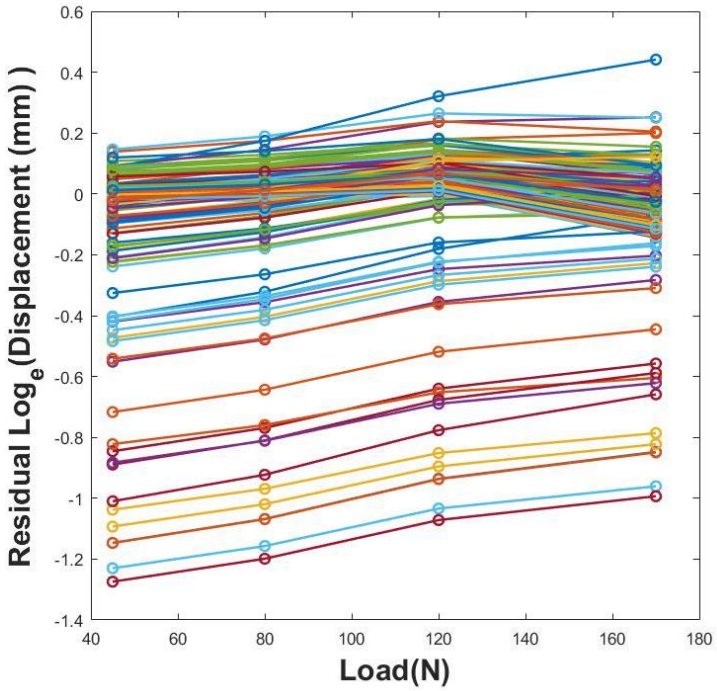

Figure 23. Surrogate model hold-out residuals for Training Plan 2

We can also compare the performance of the predictive model against results using Training Plan 1. In Figure 23, we compare the surrogate model response and overall system prediction between the two training schemes when predicting for 27%, 37%, 47%, 57%, and 67% nylon volume percentages. The bounds here also represent the prediction uncertainties and are detailed in Table 6 and Table 7 respectively for Training Plan 1 and Training Plan 2.

As seen in Figure 23 (a) and Table 6, the surrogate model responses using Training Plan 2 has significantly larger uncertainty for all results. For example at 45 N, the average bound width among five beams is 0.17 log displacement for Training Plan 1, while when using Training Plan 2, this width increases to 0.42. This indicates that the surrogate model is not able to sufficiently describe the physical behavior when the six simulation runs in Figure 20 are excluded from the training scheme. This inadequacy in the surrogate model means that the predictions have to rely heavily on corrections coming from the discrepancy term. When observing Figure 23 (b) and Table 7, this discrepancy correction is very clear, where the uncertainties in the predictions are significantly

reduced. The predictions are also a very close match to what we see when using Training Plan 1. This indicates that despite the even more limited training data, we are still able to achieve an accurate representation of the physical behavior.

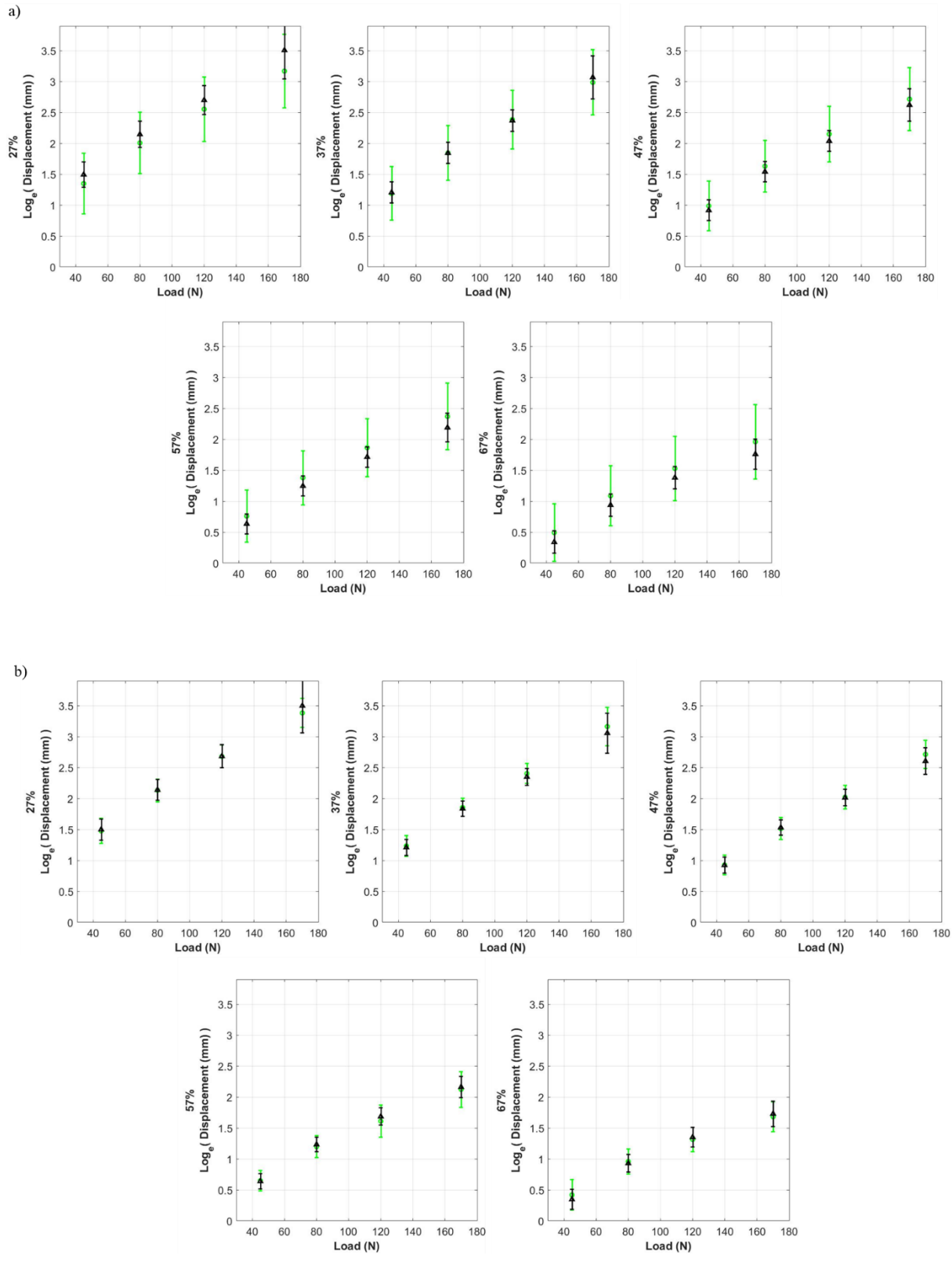

Figure 24. (a) 5th and 95th percentile bounds for surrogate model responses using Training Plan 1 (black) and Training Plan 2 (green) for the 27%, 37%, 47%, 57%, and 67% nylon (b) 5th and 95th

percentile bounds for system predictions using Training Plan 1 (black) and Training Plan 2 (green) for the 27%, 37%, 47%, 57%, and 67% nylon

Table 6. The uncertainty bounds of the surrogate model responses for using 27%, 37%, 47%, 57%, and 67% nylon Training Plan 1 and Training Plan 2

	45 N		80 N		120 N		170 N	
	Training Plan 1	Training Plan 2	Training Plan 1	Training Plan 2	Training Plan 1	Training Plan 2	Training Plan 1	Training Plan 2
27%	0.20	0.48	0.20	0.49	0.21	0.52	0.46	0.59
37%	0.16	0.41	0.16	0.42	0.17	0.44	0.34	0.49
47%	0.16	0.37	0.15	0.39	0.16	0.42	0.26	0.48
57%	0.15	0.40	0.15	0.42	0.15	0.45	0.22	0.52
67%	0.17	0.45	0.17	0.46	0.18	0.50	0.23	0.58

Table 7 The uncertainty bounds of the system predictions for using 27%, 37%, 47%, 57%, and 67% nylon Training Plan 1 and Training Plan 2

	45 N		80 N		120 N		170 N	
	Training Plan 1	Training Plan 2	Training Plan 1	Training Plan 2	Training Plan 1	Training Plan 2	Training Plan 1	Training Plan 2
27%	0.17	0.19	0.16	0.18	0.19	0.18	0.44	0.23
37%	0.14	0.16	0.13	0.15	0.14	0.16	0.33	0.31
47%	0.13	0.16	0.12	0.18	0.13	0.19	0.22	0.23
57%	0.13	0.16	0.12	0.18	0.14	0.25	0.17	0.27
67%	0.16	0.24	0.15	0.20	0.16	0.20	0.20	0.24

To observe how the discrepancy model responds to the inadequacy of the simulator, $\boldsymbol{\delta}(\boldsymbol{x})$ responses were calculated at a range of 27%-77%, as shown in Figure 21. At nylon levels below 47%, it is clear that $\boldsymbol{\delta}(\boldsymbol{x})$ corrects upwards, pearking at 0.15 log displacement, at increased load settings to account for the sharp increase in displacement that is observed at these material distributions. As the volume fraction of nylon becomes higher, this upward curve is decreased and past 47% nylon, the model starts to correct downwards. This is due to the reduced observed effect that the TPU has on the mechanical behavior, where the higher nylon content leads to a more linear displacement-load response. The downward correction hits its maximum at -0.24 log displacement

at 61% nylon, where it starts to lessen. This indicates that at higher nylon volume fractions, the simulation output begins to more closely match our observations. Another important difference is that this large negative correction from the discrepancy is not observable in Training Plan 1.

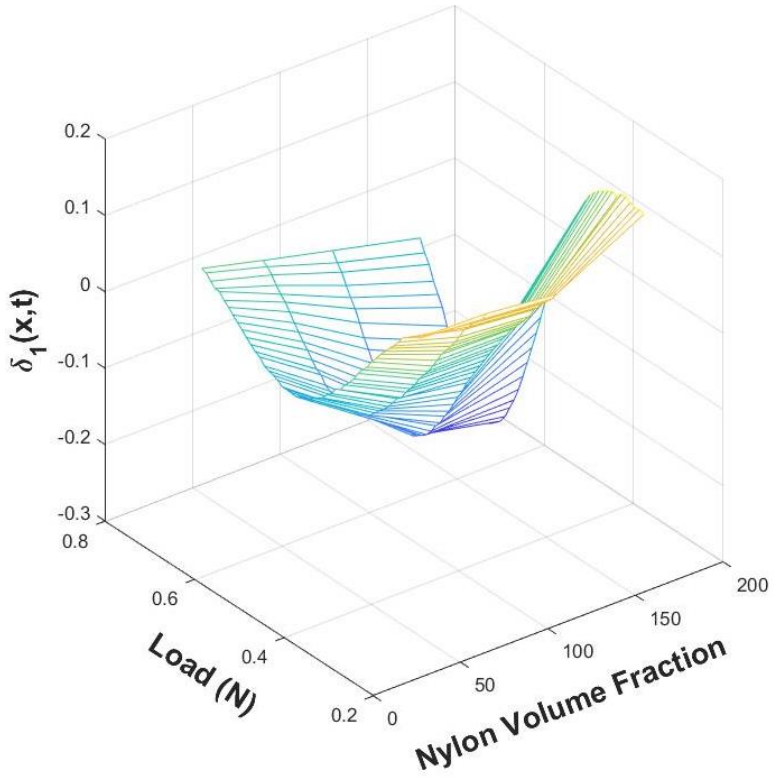

Figure 25. Posterior mean δ response as a function of material distribution

In Figure 22, the responses from both the calibrated surrogate model and the overall system prediction is shown ranging in 27% to 77% in nylon volume percentage. From comparing the two mean surfaces, the effect that posterior discrepancy has on the predictions are clear. The load-displacement behavior observed from the surrogate model response changes almost linearly across all material distributions. This is not the case for the system predictions where the upward and downward corrections can clearly be seen at increased loads. From the results of Training Plan 2, we observe that it is possible that the discrepancy model can account for the limitations present in the simulation output and closely match the physical response of our material.

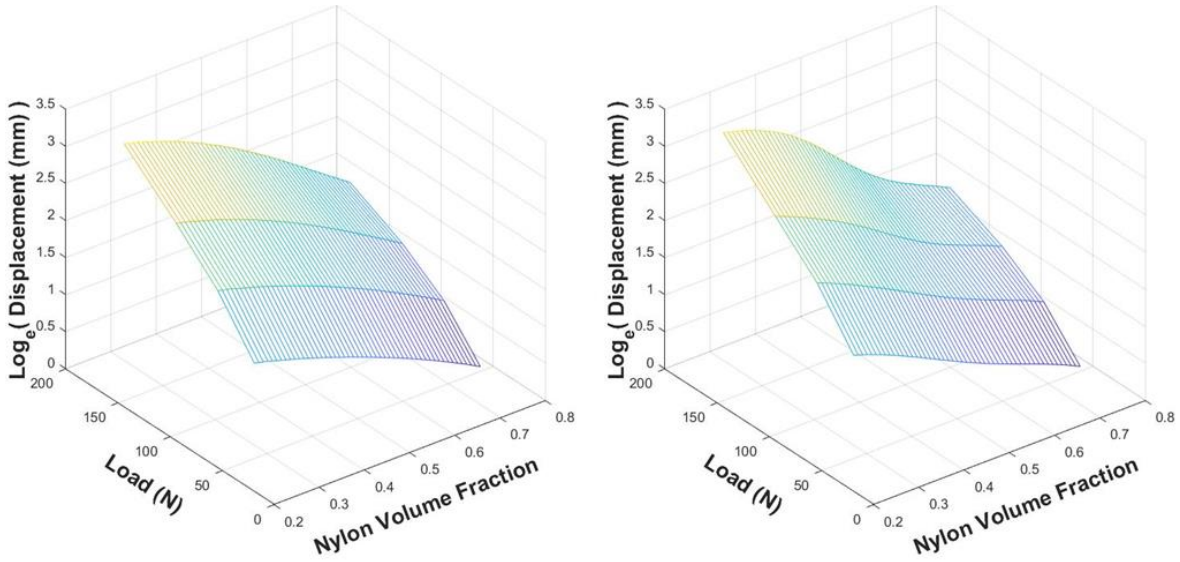

Figure 26. Posterior mean surfaces of calibrated surrogate model (left) and system prediction (right)

Chapter 5: Conclusions

A Bayesian inference-based calibration framework, integrating physical observations and simulations, was successfully implemented into our mesoscale heterogeneous material problem, which additionally provided the capability of fast prediction of the material system in response to three-point bending. Using the quantified uncertainties in our calibration parameters, we were able to obtain predictions with uncertainty. We validate our model using a hold-out procedure, confirming our accuracy despite limitations in the training data. The computational cost is significantly reduced by implementing the GP surrogate model instead of relying solely on FEA simulations.

The calibration results determined that E, C_{10}, and C_{01}, where the Young's modulus corresponds to the linear elastic model and C_{10} and C_{01} correspond to the Mooney-Rivlin model, were the inputs the simulation output had the highest dependency on based on spatial dependence parameter realizations and sensitivity analysis. We were also able to determine if any interactions between the calibration inputs were present.

The effectiveness of the discrepancy model, which accounts for the inadequacy within the simulator, was explored by adjusting the training data scheme. We introduced a second training plan where six characteristic simulation runs were removed. Despite this, the model was able to provide a realistic prediction of the mechanical behavior using the discrepancy corrections.

We aim to apply this framework further into solving the problem of multi-material design, and for more complex future material model calibration problems. The use of basis representation can be translated to problems that involve simulation data with high dimensions.

Resources

[1] I. Gibson and D. Rosen, *Additive Manufacturing Technologies*. .

[2] A. Gebhardt, *Understanding Additive Manufacturing*. Carl Hanser Verlag GmbH & Co. KG, 2011.

[3] N. Hopkinson, R. J. M. Hague, and P. M. Dickens, *Rapid Manufacturing: An Industrial Revolution for the Digital Age*. John Wiley & Sons, Ltd, 2006.

[4] D. Garcia, M. E. Jones, Y. Zhu, and H. Z. Yu, "Mesoscale design of heterogeneous material systems in multi-material additive manufacturing," *J. Mater. Res.*, vol. 33, no. 1, pp. 58–67, 2018.

[5] S. Torquato, "Optimal Design of Heterogeneous Materials," *Annu. Rev. Mater. Res.*, vol. 40, no. 1, pp. 101–129, 2010.

[6] Torquato, *Random Heterogeneous Materials: Microstructure and Macroscopic Properties*, vol. XXXIII, no. 2. 2012.

[7] H. Z. Yu, S. R. Cross, and C. A. Schuh, "Mesostructure optimization in multi-material additive manufacturing: a theoretical perspective," *J. Mater. Sci.*, vol. 52, no. 8, pp. 4288–4298, 2017.

[8] S. R. Cross, R. Woollam, S. Shademan, and C. A. Schuh, "Computational design and optimization of multilayered and functionally graded corrosion coatings," *Corros. Sci.*, vol. 77, pp. 297–307, 2013.

[9] A. T. Gaynor and J. K. Guest, "Topology optimization considering overhang constraints: Eliminating sacrificial support material in additive manufacturing through design," *Struct. Multidiscip. Optim.*, vol. 54, no. 5, pp. 1157–1172, 2016.

[10] M. Osanov and J. K. Guest, "Topology Optimization for Architectured Materials Design," *Annu. Rev. Mater. Res.*, vol. 46, pp. 211–233, 2016.

[11] H. Fudouzi, "Tunable structural color in organisms and photonic materials for design of bioinspired materials," *Sci. Technol. Adv. Mater.*, vol. 12, no. 6, 2011.

[12] R. Seidel *et al.*, “Ultrastructural and developmental features of the tessellated endoskeleton of elasmobranchs (sharks and rays),” *J. Anat.*, vol. 229, no. 5, pp. 681–702, 2016.

[13] L. J. Gibson, “The hierarchical structure and mechanics of plant materials,” *J. R. Soc. Interface*, vol. 9, no. 76, pp. 2749–2766, 2012.

[14] C. Link, “The structure and mechanics of Moso bamboo material Accessed,” 2015.

[15] J. Tsenn, J. S. Linsey, and D. A. Mcadams, “Bioinspired Materials Design: An Assessment of Methods to Improve a Text Mining Algorithm for Identifying Biological Material Structural Design Principles,” pp. 1–10, 2016.

[16] R. S. Seoudi, A. Dowd, B. J. Smith, and A. Mechler, “Structural analysis of bioinspired nano materials with synchrotron far IR spectroscopy,” *Phys. Chem. Chem. Phys.*, vol. 18, no. 16, pp. 11467–11473, 2016.

[17] R. M. Mahamood and E. T. Akinlabi, *Functionally Graded Materials*. 2017.

[18] G. Verma, “Functionally Graded Materials,” *Concise Encycl. Self-Propagating High-Temperature Synth.*, vol. 7, no. 4, pp. 135–137, 2017.

[19] Z. H. Jin and R. C. Batra, “Some basic fracture mechanics concepts in functionally graded materials,” *J. Mech. Phys. Solids*, vol. 44, no. 8, pp. 1221–1235, 1996.

[20] Z. Jin and G. Paulino, “Transient Thermal Stress Analysis of an Edge Crack in a Functionally Graded Material,” *Int. J. Fract.*, no. 107, pp. 73–98, 2001.

[21] M. C. Kennedy and A. O. Hagan, “Bayesian calibration of computer models,” pp. 425–465, 2001.

[22] M. R. Karamooz Ravari, M. Kadkhodaei, M. Badrossamay, and R. Rezaei, “Numerical investigation on mechanical properties of cellular lattice structures fabricated by fused deposition modeling,” *Int. J. Mech. Sci.*, vol. 88, pp. 154–161, 2014.

[23] D. Higdon, J. Gattiker, B. Williams, and M. Rightley, “Computer model calibration using high dimensional output,” *J. Am. Stat. Assoc.*, vol. 103, no. 482, pp. 570–583, 2008.

[24] I. S. Choi, A. J. Detor, R. Schwaiger, M. Dao, C. A. Schuh, and S. Suresh, “Mechanics of

indentation of plastically graded materials-II: Experiments on nanocrystalline alloys with grain size gradients," *J. Mech. Phys. Solids*, vol. 56, no. 1, pp. 172–183, 2008.

[25] H. Bikas, P. Stavropoulos, and G. Chryssolouris, "Additive manufacturing methods and modelling approaches : a critical review," pp. 389–405, 2016.

[26] A. Nadernezhad *et al.*, "Multifunctional 3D printing of heterogeneous hydrogel structures," *Sci. Rep.*, vol. 6, no. August, pp. 1–12, 2016.

[27] M. Müller, Q. U. Huynh, E. Uhlmann, and M. H. Wagner, "Study of inkjet printing as additive manufacturing process for gradient polyurethane material," *Prod. Eng.*, vol. 8, no. 1–2, pp. 25–32, 2014.

[28] I. Todd, "Design for additive manufacturing with site-speci fi c properties in metals and alloys," *Scr. Mater.*, vol. 135, pp. 105–110, 2017.

[29] R. Banerjee, P. C. Collins, D. Bhattacharyya, S. Banerjee, and H. L. Fraser, "Microstructural evolution in laser deposited compositionally graded α/β titanium-vanadium alloys," *Acta Mater.*, vol. 51, no. 11, pp. 3277–3292, 2003.

[30] V. K. Balla, P. D. DeVasConCellos, W. Xue, S. Bose, and A. Bandyopadhyay, "Fabrication of compositionally and structurally graded Ti-TiO2 structures using laser engineered net shaping (LENS)," *Acta Biomater.*, vol. 5, no. 5, pp. 1831–1837, 2009.

[31] U. Savitha, G. Jagan Reddy, A. Venkataramana, A. Sambasiva Rao, A. A. Gokhale, and M. Sundararaman, "Chemical analysis, structure and mechanical properties of discrete and compositionally graded SS316-IN625 dual materials," *Mater. Sci. Eng. A*, vol. 647, pp. 344–352, 2015.

[32] Y. Yan, Z. Xiong, Y. Hu, S. Wang, R. Zhang, and C. Zhang, "Layered manufacturing of tissue engineering scaffolds via multi-nozzle deposition," *Mater. Lett.*, vol. 57, no. 18, pp. 2623–2628, 2003.

[33] R. M. Pidaparti, *Engineering Finite Element Analysis*, vol. 1, no. 1. 2017.

[34] O. C. Zienkiewicz, R. L. Taylor, and J. Z. Zhu, "The Standard Discrete System and Origins of the Finite Element Method," *Finite Elem. Method its Basis Fundam.*, pp. 1–20,

2013.

[35] D. Coutellier and P. Rozycki, “Multi-layered multi-material finite element for crashworthiness studies,” vol. 31, pp. 841–851, 2000.

[36] L. M. Xu, H. Fan, K. Y. Sze, and C. Li, “Elastic property prediction by finite element analysis with random distribution of materials for heterogeneous solids,” *Int. J. Mech. Mater. Des.*, vol. 3, no. 4, pp. 319–327, 2006.

[37] V. Sarhosis, “An optimization procedure for material parameter identification in masonry constitutive models . International Journal of Masonry Research An optimization procedure for material parameter identification for masonry constitutive models,” vol. 1, no. August, pp. 48–58, 2016.

[38] C. S. Desai and J. Y. Chen, “Parameter optimization and sensitivity analysis for disturbed state constitutive model,” *Int. J. Geomech.*, vol. 6, no. 2, pp. 75–88, 2006.

[39] C. Y. Tang, G. Y. F. Ng, Z. W. Wang, G. C. P. Tsui, and G. Zhang, “Parameter optimization for the visco-hyperelastic constitutive model of tendon using FEM,” *Biomed. Mater. Eng.*, vol. 21, no. 1, pp. 9–24, 2011.

[40] N. E. Karkalos and A. P. Markopoulos, “Determination of Johnson-Cook material model parameters by an optimization approach using the fireworks algorithm,” *Procedia Manuf.*, vol. 22, pp. 107–113, 2018.

[41] C. Cekerevac, S. Girardin, G. Klubertanz, and L. Laloui, “Calibration of an elasto-plastic constitutive model by a constrained optimisation procedure,” *Comput. Geotech.*, vol. 33, no. 8, pp. 432–443, 2006.

[42] V. Sarhosis and Y. Sheng, “Identification of material parameters for low bond Identification of material parameters for modeling of masonry structures,” no. January 2015, pp. 100–110, 2016.

[43] H. Xie and Y. Kang, “Digital image correlation technique,” *Opt. Lasers Eng.*, vol. 65, pp. 1–2, 2014.

[44] N. McCormick and J. Lord, “Digital image correlation,” *Mater. Today*, vol. 13, no. 12, pp.

52–54, 2010.

[45] T. C. Chu, W. F. Ranson, and M. A. Sutton, “Applications of digital-image-correlation techniques to experimental mechanics,” *Exp. Mech.*, vol. 25, no. 3, pp. 232–244, 1985.

[46] B. Pan, K. Qian, H. Xie, and A. Asundi, “Two-dimensional digital image correlation for in-plane displacement and strain measurement: A review,” *Meas. Sci. Technol.*, vol. 20, no. 6, 2009.

[47] B. Pan, “Recent Progress in Digital Image Correlation,” *Exp. Mech.*, vol. 51, no. 7, pp. 1223–1235, 2011.

[48] Y. Su, Z. Gao, Q. Zhang, and S. Wu, “Spatial uncertainty of measurement errors in digital image correlation,” *Opt. Lasers Eng.*, vol. 110, no. May, pp. 113–121, 2018.

[49] T. Stankovic, J. Mueller, P. Egan, and K. Shea, “A Generalized Optimality Criteria Method for Optimization of Additively Manufactured Multimaterial Lattice Structures,” *J. Mech. Des.*, vol. 137, no. 11, p. 111405, 2015.

[50] B. P. Carlin, T. A. Louis, and P. Bradley, *BAYES AND EMPIRICAL BAYES METHODS FOR Second edition*. .

[51] H. L. Harney, “Bayesian inference: Data evaluation and decisions,” *Bayesian Inference Data Eval. Decis.*, pp. 1–243, 2016.

[52] J. E. Oakley, A. O. Hagan, and A. O’Hagan, “Probabilistic sensitivity analysis of complex models : a Bayesian approach,” *J. R. Stat. Soc. Ser. B Stat. Methodol.*, vol. 66, no. 3, pp. 751–769, 2004.

[53] J. Oakley and A. O. Hagan, “Biometrika Trust Bayesian Inference for the Uncertainty Distribution of Computer Model Outputs Published by : Oxford University Press on behalf of Biometrika Trust Stable URL : http://www.jstor.org/stable/4140536 Linked references are available on JSTOR f,” vol. 89, no. 4, pp. 769–784, 2017.

[54] C. E. Coleman-Smith, “Using Gaussian Processes for the Calibration and Exploration of Complex Computer Models,” 2014.

[55] C. Rasmussen, W. Edward, and C. K. I., *Gaussian Processes for Machine Learning*.

Cambridge, Mass: The MIT Press, 2006.

[56] G. H. Golub, V. Loan, and C. F., *Matrix Computations*. Baltimore: The Johns Hopkin University Press, 2013.

[57] J. Sacks, W. J. Welch, J. Mitchell, and H. P. Wynn, *Design and analysis of comuter experiments*. Statistical Science, 1989.

[58] N. Cressie, *Statistics for Spatial Data*. Wiley, 1992.

[59] M. Stein, *Interpolation of Spatial Data: Some Theory for Kriging*. Springer, 1999.

[60] B. Ripley, *Spatial Statistics*. Wiley, 1989.

[61] T. Santner, B. Williams, and W. Notz, *The design and analysis of computer experiments*. 2003.

[62] R. Kannan and J. Hopcroft, "Computer Science Theory for the Information Age," *Comput. Sci. Theory Inf. Age*, pp. 270–278, 2012.

[63] G. Strang, *Linear Algebra and Its Applications*, 4th ed. Belmont, CA: Thomson, Brooks/Cole, 2006.

[64] W. Chang, M. Haran, R. Olson, and K. Keller, "Fast dimension-reduced climate model calibration and the effect of data aggregation," *Ann. Appl. Stat.*, vol. 8, no. 2, pp. 649–673, 2014.

[65] A. M. J. Bayarri *et al.*, "Computer Model Validation with Functional Output," vol. 35, no. 5, pp. 1874–1906, 2007.

[66] C. Andrieu, "An Introduction to MCMC for Machine Learning," pp. 5–43, 2003.

[67] A. F. M. Smith and G. O. Roberts, "Bayesian Computation Via the Gibbs Sampler and Related Markov Chain Monte Carlo Methods," *J. R. Stat. Soc.*, vol. 55, no. 1, pp. 3–23, 1993.

[68] N. Metropolis, A. W. Rosenbluth, M. N. Rosenbluth, A. H. Teller, and E. Teller, "Equation of State Calculations by Fast Computing Machines," vol. 1087, 1953.

[69] D. Gamerman and H. F. Lopes, *Markov Chain Monte Carlo Stochastic Simulation for*

Bayesian Inference, 2nd ed. Chapman & Hall/CRC, 2006.

[70] S. Brooks, A. Gelman, G. L. Jones, and X.-L. Meng, *Handbook of Markov Chain Monte Carlo*, 1st ed. Chapman & Hall/CRC, 2011.

[71] A. E. Gelfand, "Gibbs Sampling," *J. Am. Stat. Assoc.*, vol. 95, no. 452, pp. 1300–1304, 2000.

[72] W. K. Hastings, "Monte Carlo Sampling Methods Using Markov Chains and Their Applications," *Biometrika*, vol. 57, no. 1, pp. 97–109, 1970.

[73] A. F. Bower, *Applied Mechanics of Solids*. 2010.

[74] R. Society and P. Sciences, "Large Elastic Deformations of Isotropic Materials . I . Fundamental Concepts Author (s): R . S . Rivlin Source : Philosophical Transactions of the Royal Society of London . Series A , Mathematical Published by : Royal Society Stable URL : http://www.jst," vol. 240, no. 822, pp. 459–490, 2018.

[75] W. E. King *et al.*, "Laser powder bed fusion additive manufacturing of metals; physics, computational, and materials challenges," *Appl. Phys. Rev.*, vol. 2, no. 4, p. 041304, 2015.

[76] W. E. King *et al.*, "Observation of keyhole-mode laser melting in laser powder-bed fusion additive manufacturing," *J. Mater. Process. Technol.*, vol. 214, no. 12, pp. 2915–2925, 2014.

[77] W. J. Sames, F. A. List, S. Pannala, R. R. Dehoff, and S. S. Babu, "The metallurgy and processing science of metal additive manufacturing," *Int. Mater. Rev.*, vol. 61, no. 5, pp. 315–360, 2016.

[78] J. Bergström, *Mechanics of Solid Polymers - Theory and Computational Modeling - Knovel*. 2015.